














# TECH BRIEFS

NATIONAL AERONAUTICS AND SPACE ADMINISTRATION

-  **Technology Focus**
-  **Computers/Electronics**
-  **Software**
-  **Materials**
-  **Mechanics**
-  **Machinery/Automation**
-  **Manufacturing**
-  **Bio-Medical**
-  **Physical Sciences**
-  **Information Sciences**
-  **Books and Reports**



## INTRODUCTION

Tech Briefs are short announcements of innovations originating from research and development activities of the National Aeronautics and Space Administration. They emphasize information considered likely to be transferable across industrial, regional, or disciplinary lines and are issued to encourage commercial application.

### Availability of NASA Tech Briefs and TSPs

Requests for individual Tech Briefs or for Technical Support Packages (TSPs) announced herein should be addressed to

#### National Technology Transfer Center

Telephone No. (800) 678-6882 or via World Wide Web at [www2.nttc.edu/leads/](http://www2.nttc.edu/leads/)

Please reference the control numbers appearing at the end of each Tech Brief. Information on NASA's Commercial Technology Team, its documents, and services is also available at the same facility or on the World Wide Web at [www.nctn.hq.nasa.gov](http://www.nctn.hq.nasa.gov).

Commercial Technology Offices and Patent Counsels are located at NASA field centers to provide technology-transfer access to industrial users. Inquiries can be made by contacting NASA field centers and program offices listed below.

## NASA Field Centers and Program Offices

#### Ames Research Center

Carolina Blake  
(650) 604-1754  
[cblake@mail.arc.nasa.gov](mailto:cblake@mail.arc.nasa.gov)

#### Dryden Flight Research Center

Jenny Baer-Riedhart  
(661) 276-3689  
[jenny.baer-riedhart@dfrc.nasa.gov](mailto:jenny.baer-riedhart@dfrc.nasa.gov)

#### Goddard Space Flight Center

Nona Cheeks  
(301) 286-5810  
[Nona.K.Cheeks.1@gsfc.nasa.gov](mailto:Nona.K.Cheeks.1@gsfc.nasa.gov)

#### Jet Propulsion Laboratory

Art Murphy, Jr.  
(818) 354-3480  
[arthur.j.murphy-jr@jpl.nasa.gov](mailto:arthur.j.murphy-jr@jpl.nasa.gov)

#### Johnson Space Center

Charlene E. Gilbert  
(281) 483-3809  
[commercialization@jsc.nasa.gov](mailto:commercialization@jsc.nasa.gov)

#### Kennedy Space Center

Jim Aliberti  
(321) 867-6224  
[Jim.Aliberti-1@ksc.nasa.gov](mailto:Jim.Aliberti-1@ksc.nasa.gov)

#### Langley Research Center

Sam Morello  
(757) 864-6005  
[s.a.morello@larc.nasa.gov](mailto:s.a.morello@larc.nasa.gov)

#### John H. Glenn Research Center at Lewis Field

Larry Viterna  
(216) 433-3484  
[cto@grc.nasa.gov](mailto:cto@grc.nasa.gov)

#### Marshall Space Flight Center

Vernotto McMillan  
(256) 544-2615  
[vernotto.mcmillan@msfc.nasa.gov](mailto:vernotto.mcmillan@msfc.nasa.gov)

#### Stennis Space Center

Robert Bruce  
(228) 688-1929  
[robert.c.bruce@nasa.gov](mailto:robert.c.bruce@nasa.gov)

#### NASA Program Offices

At NASA Headquarters there are seven major program offices that develop and oversee technology projects of potential interest to industry:

##### Carl Ray

Small Business Innovation  
Research Program (SBIR) &  
Small Business Technology  
Transfer Program (STTR)  
(202) 358-4652 or  
[cray@mail.hq.nasa.gov](mailto:cray@mail.hq.nasa.gov)

##### Dr. Robert Norwood

Office of Commercial  
Technology (Code RW)  
(202) 358-2320 or  
[rnorwood@mail.hq.nasa.gov](mailto:rnorwood@mail.hq.nasa.gov)

##### John Mankins

Office of Space Flight (Code MP)  
(202) 358-4659 or  
[jmankins@mail.hq.nasa.gov](mailto:jmankins@mail.hq.nasa.gov)

##### Terry Hertz

Office of Aero-Space  
Technology (Code RS)  
(202) 358-4636 or  
[thertz@mail.hq.nasa.gov](mailto:thertz@mail.hq.nasa.gov)

##### Glen Mucklow

Office of Space Sciences  
(Code SM)  
(202) 358-2235 or  
[gmucklow@mail.hq.nasa.gov](mailto:gmucklow@mail.hq.nasa.gov)

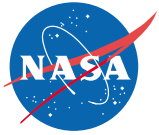
##### Roger Crouch

Office of Microgravity Science  
Applications (Code U)  
(202) 358-0689 or  
[rcrouch@hq.nasa.gov](mailto:rcrouch@hq.nasa.gov)

##### Granville Paules

Office of Mission to Planet Earth  
(Code Y)  
(202) 358-0706 or  
[gpaules@mtpe.hq.nasa.gov](mailto:gpaules@mtpe.hq.nasa.gov)





# TECH BRIEFS

NATIONAL AERONAUTICS AND SPACE ADMINISTRATION



## 5 Technology Focus: Data Acquisition

- 5 Real-Time, High-Frequency QRS Electrocardiograph
- 6 Software for Improved Extraction of Data From Tape Storage
- 6 Radio System for Locating Emergency Workers
- 7 Software for Displaying High-Frequency Test Data



## 9 Computers/Electronics

- 9 Capacitor-Chain Successive-Approximation ADC
- 10 Simpler Alternative to an Optimum FQPSK-B Viterbi Receiver
- 11 Multilayer Patch Antenna Surrounded by a Metallic Wall



## 13 Software

- 13 Software To Secure Distributed Propulsion Simulations



## 15 Materials

- 15 Explicit Pore Pressure Material Model in Carbon-Cloth Phenolic
- 16 Meshed-Pumpkin Super-Pressure Balloon Design
- 17 Corrosion Inhibitors as Penetrant Dyes for Radiography
- 17 Transparent Metal-Salt-Filled Polymeric Radiation Shields



## 19 Mechanics

- 19 Lightweight Energy Absorbers for Blast Containers
- 19 Brush-Wheel Samplers for Planetary Exploration



## 21 Manufacturing

- 21 Dry Process for Making Polyimide/Carbon-and-Boron-Fiber Tape
- 21 Relatively Inexpensive Rapid Prototyping of Small Parts



## 23 Physical Sciences

- 23 Magnetic Field Would Reduce Electron Backstreaming in Ion Thrusters
- 24 Alternative Electrochemical Systems for Ozonation of Water
- 25 Interferometer for Measuring Displacement to Within 20 pm
- 26 UV-Enhanced IR Raman System for Identifying Biohazards



## 29 Information Sciences

- 29 Prognostics Methodology for Complex Systems
- 30 Algorithms for Haptic Rendering of 3D Objects
- 31 Modeling and Control of Aerothermoelastic Effects
- 32 Processing Digital Imagery to Enhance Perceptions of Realism



## 33 Books & Reports

- 33 Analysis of Designs of Space Laboratories
- 33 Shields for Enhanced Protection Against High-Speed Debris
- 33 Study of Dislocation-Ordered  $\text{In}_x\text{Ga}_{1-x}\text{As}/\text{GaAs}$  Quantum Dots
- 33 Tilt-Sensitivity Analysis for Space Telescopes

This document was prepared under the sponsorship of the National Aeronautics and Space Administration. Neither the United States Government nor any person acting on behalf of the United States Government assumes any liability resulting from the use of the information contained in this document, or warrants that such use will be free from privately owned rights.





## Real-Time, High-Frequency QRS Electrocardiograph

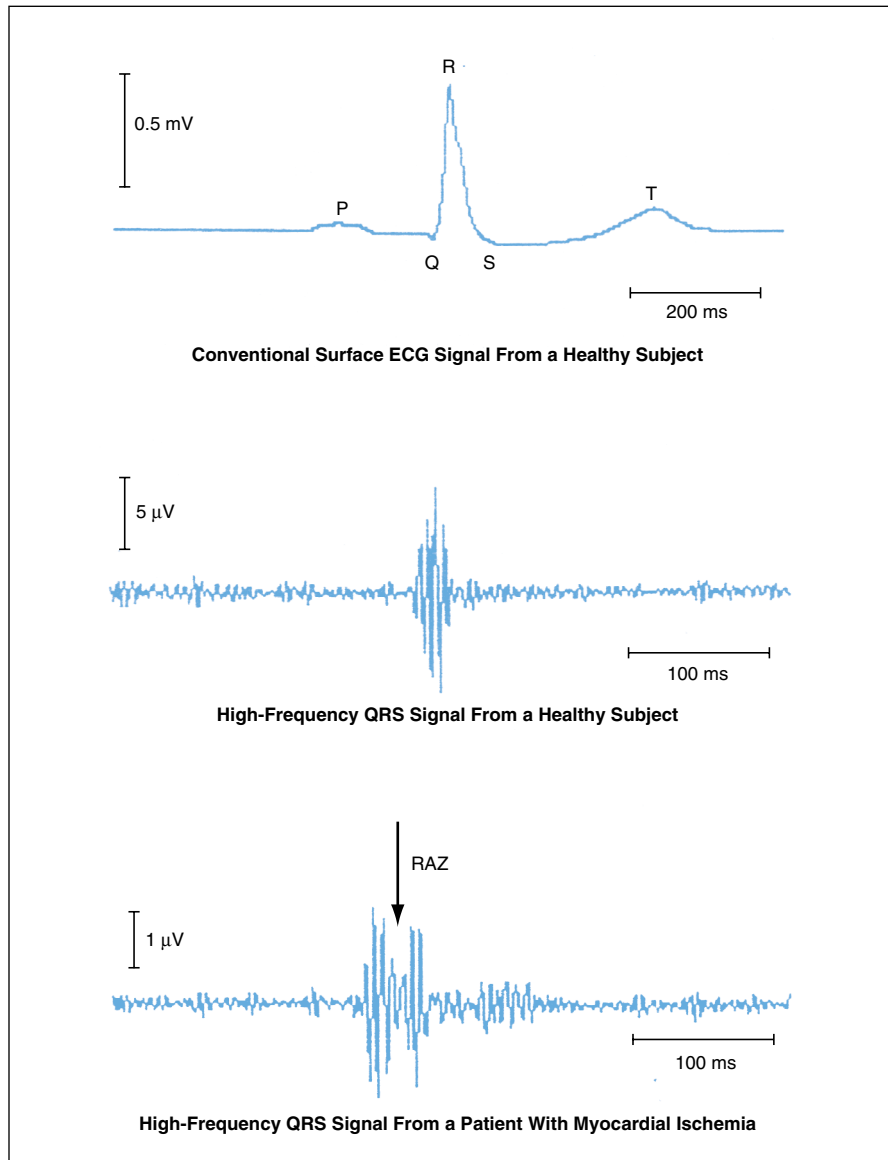
Signals indicative of ischemia or infarction can be identified in real time.

Lyndon B. Johnson Space Center, Houston, Texas

An electronic system that performs real-time analysis of the low-amplitude, high-frequency, ordinarily invisible components of the QRS portion of an electrocardiographic signal in real time has been developed. Whereas the signals readily visible on a conventional electrocardiogram (ECG) have amplitudes of the order of a millivolt and are characterized by frequencies  $<100$  Hz, the ordinarily invisible components have amplitudes in the microvolt range and are characterized by frequencies from about 150 to about 250 Hz. Deviations of these high-frequency components from a normal pattern can be indicative of myocardial ischemia or myocardial infarction (see figure).

Prior to the development of this system, analyses of the high-frequency components of QRS signals entailed laborious, time-consuming post-measurement calculations and thus had research value only: they did not provide data quickly enough to provide guidance for clinical decisions for treating cardiac patients at immediate risk. The ability to provide clinically relevant information in real time makes the present system a prototype of a superior QRS electrocardiograph that could find its way into nearly every emergency room, ambulance, intensive-care unit, surgical operating room, cardiac hospital ward, cardiac-exercise/ECG testing facility, and cardiac-catheterization laboratory.

The system includes standard electrocardiograph electrodes, which are connected to high-input-impedance field-effect-transistor (FET) leads. The outputs of the FET leads are fed to a preamplifier, the output of which is fed to a data-acquisition circuit card in the Personal Computer Memory Card International Association (PCMCIA) slot in a personal computer. The card digitizes the electrocardiographic signal at a sampling rate of 1,000 Hz. The data thus acquired by the card are analyzed by special-purpose software running in a Windows operating system. Optionally, the data can be stored in a file for subsequent playback and analysis.



The **High-Frequency Signal Components** are invisible in a conventional surface electrocardiogram. These components can be extracted by filtering. A reduced-amplitude zone (RAZ) like the one shown in the lowermost plot may be indicative of dead or ischemic cardiac conduction tissue.

Whether processing real-time or previously recorded data, the special-purpose software performs several functions. The software detects R waves and QRS complexes and analyzes them from several perspectives. A conventional, unfiltered, beat-to-beat limb-lead ECG signal with an amplitude of the order of a millivolt is shown run-

ning across a window at the top of the computer screen. The software also computes and displays a signal that is similar except that it has been averaged over a number (selectable by the user) of consecutive beats in order to increase the signal-to-noise ratio.

The software includes a provision for special-purpose non-recursive digi-

tal filters with varying low- and high-frequency cutoffs. These filters, applied to the averaged signal, effect a band-pass operation in the frequency range from 150 to 250 Hz. The output of the band-pass filter is the desired high-frequency QRS signal. Further processing is then performed to obtain the power spectrum of the filtered sig-

nal, the beat-to-beat root mean square (rms) voltage amplitude of the filtered signal, certain variations of the rms voltage, and such standard measures as the heart rate and R-R interval at any given time.

*This work was done by Todd T. Schlegel of Johnson Space Center, Jude L. DePalma of Texas A & M University, and Saeed*

*Moradi of Eix, Inc. Further information is contained in a TSP (see page 1).*

*This invention is owned by NASA, and a patent application has been filed. Inquiries concerning nonexclusive or exclusive license for its commercial development should be addressed to the Patent Counsel, Johnson Space Center, (281) 483-0837. Refer to MSC-23154.*

---

## Software for Improved Extraction of Data From Tape Storage

*Stennis Space Center, Mississippi*

A computer program has been written to replace the original software of Racal Storeplex Delta tape recorders, which are used at Stennis Space Center. The original software could be activated by a command-line interface only; the present software offers the option of a command-line or graphical user interface. The present software also offers the option of batch-file operation (activation by a file that contains command lines for operations

performed consecutively). The present software is also more reliable than was the original software: The original software was plagued by several deficiencies that made it difficult to execute, modify, and test. In addition, when using the original software to extract data that had been recorded within specified intervals of time, the resolution with which one could control starting and stopping times was no finer than about a second (or, in some

cases, several seconds). In contrast, the present software is capable of controlling playback times to within 1/100 second of times specified by the user, assuming that the tape-recorder clock is accurate to within 1/100 second.

*This program was written by Chiu-Fu Cheng of Lockheed Martin Corp. for Stennis Space Center. For further information, contact the Stennis Commercial Technology Office at (228) 688-1929. SSC-00156*

---

## Radio System for Locating Emergency Workers

**Locations and identities of workers are tracked in real time.**

*John F. Kennedy Space Center, Florida*

A system based on low-power radio transponders and associated analog and digital electronic circuitry has been developed for locating firefighters and other emergency workers deployed in a building or other structure. The system has obvious potential for saving lives and reducing the risk of injuries.

The system includes (1) a central station equipped with a computer and a transceiver; (2) active radio-frequency (RF) identification tags, each placed in a different room or region of the structure; and (3) transponder units worn by the emergency workers. The RF identification tags can be installed in a new building as built-in components of standard fire-detection devices or ground-fault electrical outlets or can be attached to such devices in a previously constructed building, without need for rewiring the building. Each RF identification tag contains information that uniquely identifies it. When each tag is installed, information on its location and identity are reported to, and stored at, the central station. In an emergency, if a building has not been prewired with

RF identification tags, leading emergency workers could drop sequentially numbered portable tags in the rooms of the building, reporting the tag numbers and locations by radio to the central station as they proceed.

Each RF identification tag periodically transmits a short-burst, low-power signal containing its unique identifier code. The intervals between these transmissions are made pseudorandom to minimize interference among transmissions from different RF identification tags. Each emergency worker wears a transponder unit, which receives the codes transmitted by one or more RF identification tag(s) and measures their relative signal strengths. Each transponder also transmits a unique identifier code, which makes it possible to distinguish its wearer from other emergency workers.

The central station periodically transmits a polling command, in response to which each transponder transmits its identification code plus all of the RF-identification-tag information it has received during the preceding 5 seconds.

For each such polling cycle, the central station issues only one polling command, and each transponder responds during a unique assigned time slot after that command, as determined by its code: this arrangement minimizes the "handshaking" needed to establish communication with transponders and reduces the cycle time for the location updates. On the basis of the relative strengths of RF-identification-tag signals reported by each transponder and the locations of the tags that transmitted those signals, the central-station computer calculates the location of the transponder and, hence, of the emergency worker who carries it. Thus, the locations of all emergency workers are repeatedly updated and displayed in real time at the central station.

The power for prewired RF identification tags is derived from the main AC power of the building by means of a rectifier/voltage-divider circuit, which also maintains a charge in a miniature, large-capacitance capacitor. The power demand of the RF identification tags is so low that in the likely event of loss of AC



power during an emergency, the tags can continue to operate for at least 72 hours from the charge stored in the capacitor.

The design of the RF identification tags is based on a microcontroller chip. This design is amenable to easy and inexpensive integration of sensors. For instance, digital temperature sensors could be included within the RF identification tags. In that case, the information provided to the central station

could also include the temperature of the wall, roof, or other portion of the structure where the tag is located. The temperature would be an additional indication of the integrity of the structure and progress of a fire through the building. The RF identification tags can be encapsulated for protection against water, smoke, and shock, and can be made from components that withstand extremes of temperature.

Most of the hardware and software of

the system have been tested in a laboratory, and limited field tests have been performed. At the time of reporting the information for this article, several fire departments had expressed interest in this system.

*This work was done by William Larson of Kennedy Space Center and Pedro Medelius, Stan Starr, Guy Bedette, John Taylor, and Steve Moerk, of Dynacs Engineering Co. Further information is contained in a TSP (see page 1). KSC-12079*

---

## Software for Displaying High-Frequency Test Data

*Marshall Space Flight Center, Alabama*

An easy-to-use, intuitive computer program was written to satisfy a need of test operators and data requestors to quickly view and manipulate high-frequency test data recorded at the East and West Test Areas at Marshall Space Flight Center. By enabling rapid analysis, this program makes it possible to reduce times between test runs, thereby potentially reducing the overall cost of test operations. The program can be used to perform quick frequency analysis, using multiple fast-

Fourier-transform windowing and amplitude options. The program can generate amplitude-versus-time plots with full zoom capabilities, frequency-component plots at specified time intervals, and waterfall plots (plots of spectral intensity versus frequency at successive small time intervals, showing the changing frequency components over time). There are options for printing of the plots and saving plot data as text files that can be imported into other application programs. The program

can perform all of the aforementioned plotting and plot-data-handling functions on a relatively inexpensive computer; other software that performs the same functions requires computers with large amounts of power and memory.

*This program was written by Jason L. Elmore of Marshall Space Flight Center. For further information, contact the Marshall Commercial Technology Office at (256) 544-2615. MFS-31700*





## Capacitor-Chain Successive-Approximation ADC

This ADC could be very compact, relative to a binary-scaled successive-approximation ADC.

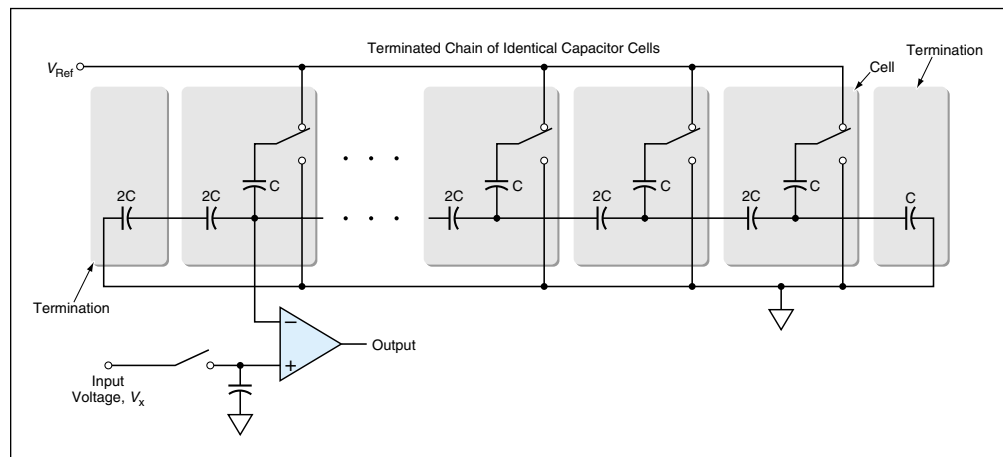
NASA's Jet Propulsion Laboratory, Pasadena, California

A proposed successive-approximation analog-to-digital converter (ADC) would contain a capacitively terminated chain of identical capacitor cells (see figure). Like a conventional successive-approximation ADC containing a bank of binary-scaled capacitors, the proposed ADC would store an input voltage on a sample-and-hold capacitor and would digitize the stored input voltage by finding the closest match between this voltage and a capacitively generated sum of binary fractions of a reference voltage ( $V_{ref}$ ). However, the proposed capacitor-chain ADC would offer two major advantages over a conventional binary-scaled-capacitor ADC:

- In a conventional ADC that digitizes to  $n$  bits, the largest capacitor (representing the most significant bit) must have  $2^{n-1}$  times as much capacitance, and hence, approximately  $2^{n-1}$  times as much area as does the smallest capacitor (representing the least significant bit), so that the total capacitor area must be  $2^n$  times that of the smallest capacitor. In the proposed capacitor-chain ADC, there would be three capacitors per cell, each approximately equal to the smallest capacitor in the conventional ADC, and there would be one cell per bit. Therefore, the total capacitor area would be only about  $3n$  times that of the smallest capacitor. The net result would be that the proposed ADC could be considerably smaller than the conventional ADC.
- Because of edge effects, parasitic capacitances, and manufacturing tolerances, it is difficult to make capacitor banks in which the values of capacitance are scaled by powers of 2 to the required precision. In contrast, because all the capacitors in the proposed ADC would be identical, the problem of precise binary scaling would not arise.

In the proposed ADC, as in the conventional capacitor-chain ADC, a sampled version of the input voltage is sent together with the capacitively generated sum of binary fractions of  $V_{ref}$  into the two input terminals of a comparator. Also as in the conventional ADC, the sum of binary fractions of  $V_{ref}$  is generated by elec-

terminated to ground via capacitors of  $2C$  and  $C$ , respectively. The chain would constitute a capacitive voltage-divider network containing switched parallel and series connections. By an algebraic derivation from basic circuit theory, it can be shown that switching from the ground connection to the  $V_{ref}$  connec-



A Capacitor-Chain Successive-Approximation ADC, shown here in simplified form, would contain a capacitively terminated chain of identical capacitor cells. A sum of binary-weighted voltages would be generated by throwing switches, starting in the leftmost cell for the most-significant bit and proceeding rightward through successive cells to the least-significant bit.

tronically switching capacitor connections between ground and  $V_{ref}$ . The comparator determines whether the generated voltage is higher or lower than the input voltage, and by switching in or out successively smaller binary fractions of  $V_{ref}$ , the ADC brackets the input voltage between successively converging binary values.

Each cell could be characterized as containing two or three capacitors, depending on one's perspective: One capacitor would have the minimum capacitance,  $C$ , while the other would have a capacitance of  $2C$ . In practice, the  $2C$  capacitor could be fabricated as two  $1C$  capacitors in parallel, so that a cell would contain three identical capacitors, of which two would be tied together.

Only the first cell would be tied directly to the inverting terminal of the comparator. The second cell would be connected to the first cell, the third cell connected to the second, and so forth, forming a chain of identical cells. The first and last cells of the chain would be

tion in each successive cell of this network would contribute the next less-significant binary fraction of  $V_{ref}$  to the input terminal of the comparator. More specifically, the voltage contribution obtained by such switching in the  $m$ th cell would be given by

$$\Delta V_n = 2^{-m}(V_{ref}/3).$$

This work was done by Thomas Cunningham of Caltech for NASA's Jet Propulsion Laboratory. Further information is contained in a TSP (see page 1).

In accordance with Public Law 96-517, the contractor has elected to retain title to this invention. Inquiries concerning rights for its commercial use should be addressed to

Intellectual Property group

JPL

Mail Stop 202-233

4800 Oak Grove Drive

Pasadena, CA 91109

(818) 354-2240

Refer to NPO-21145, volume and number of this NASA Tech Briefs issue, and the page number.

# ● Simpler Alternative to an Optimum FQPSK-B Viterbi Receiver

Performance is only slightly below that of the more-complex optimum version.

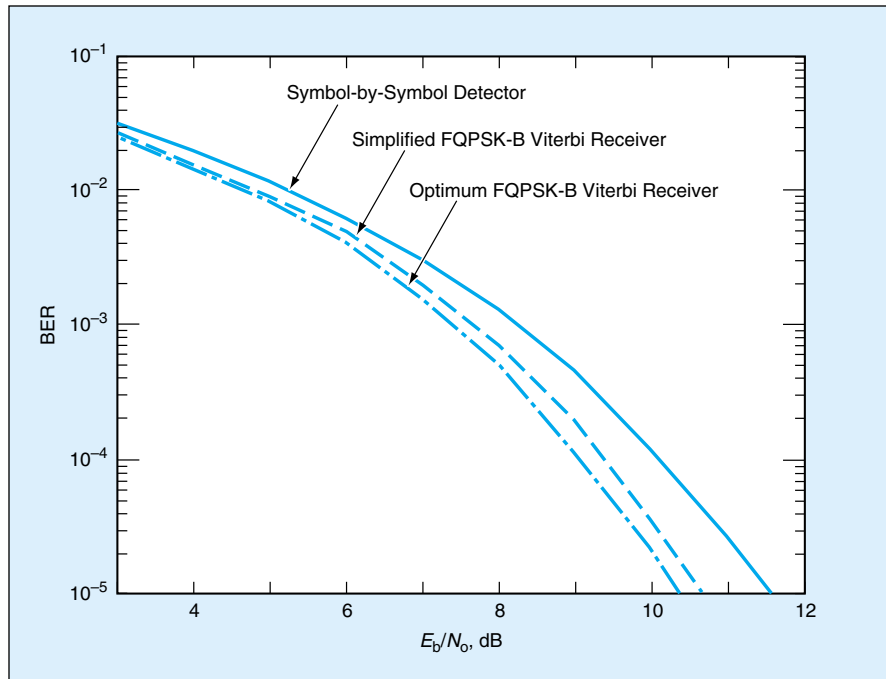
NASA's Jet Propulsion Laboratory, Pasadena, California

A reduced-complexity alternative to an optimum FQPSK-B Viterbi receiver has been invented. As described below, the reduction in complexity is achieved at the cost of only a small reduction in power performance [performance expressed in terms of a bit-energy-to-noise-energy ratio ( $E_b/N_0$ ) for a given bit-error rate (BER)].

The term "FQPSK-B" denotes a baseband-filtered version of Feher quadrature-phase-shift keying, which is a patented, bandwidth-efficient phase-modulation scheme named after its inventor. Heretofore, commercial FQPSK-B receivers have performed symbol-by-symbol detection, in each case using a detection filter (either the proprietary FQPSK-B filter for better BER performance, or a simple integrate-and-dump filter with degraded performance) and a sample-and-hold circuit.

In comparison with symbol-by-symbol detection, Viterbi demodulation (based on a trellis-coded interpretation of FQPSK) provides better BER performance because it takes advantage of the memory inherent in an FQPSK-B signal and can be designed to be optimum for demodulating FQPSK-B. In the trellis-coded interpretation, FQPSK is regarded as having been generated by transmitting one of 16 shaped waveforms (8 unique waveforms and their negatives) based on a 16-state trellis. In the decoding/demodulation process, the receiver correlates the baseband received signal with each of the 16 FQPSK waveforms and the Viterbi algorithm searches through the FQPSK trellis, which includes four transitions to each of the 16 states. To be able to implement the Viterbi algorithm, the receiver must include 16 correlators — eight for the in-phase and eight for the quadrature channel. This receiver design is likely to be too complex to be practical in typical commercial applications.

The simplified FQPSK-B Viterbi receiver is based on grouping the 16 waveforms into four groups of four waveforms each. The received FQPSK-B signal is correlated against the average of the waveforms in each group. By appropriate selection of the waveforms



Performances of Three FQPSK-B Receivers were evaluated by computational simulation.

for the groups, the trellis can be reduced from 16 states with four transitions per state to two independent two-state trellises with only two transitions per state. Due to the similarity between the FQPSK waveforms, this simpler receiver has only a small  $E_b/N_0$  penalty, compared to the full Viterbi receiver, while still offering significant performance gain relative to the FQPSK-B receiver using the proprietary FQPSK-B detection filter. The simplified FQPSK-B Viterbi receiver requires four correlators, and the amount of computation needed to generate each decoded bit is only one-eighth of that of the optimum FQPSK-B receiver.

The simplified FQPSK-B Viterbi receiver concept has been tested by computational simulation, and compared with both the optimum FQPSK-B Viterbi receiver and symbol-by-symbol detector using the FQPSK-B proprietary filter. In the simulations, ideal carrier and symbol synchronization was assumed. The simulated channel included a nonlinear solid-state power amplifier operating in full saturation. Because of the shorter constraint length of the reduced trellis, the trun-

cation path length (decoding depth) needed for the simplified FQPSK-B Viterbi receiver was only one-fifth of that needed for the optimum FQPSK-B Viterbi receiver. The results (see figure) show that the simplified FQPSK-B Viterbi receiver can be expected to perform better than the symbol-by-symbol detector using the FQPSK-B proprietary detection filter, and almost as well as does the optimum FQPSK-B Viterbi receiver.

*This work was done by Dennis Lee, Marvin Simon, and Tsun-Yee Yan of Caltech for NASA's Jet Propulsion Laboratory. Further information is contained in a TSP (see page 1).*

*In accordance with Public Law 96-517, the contractor has elected to retain title to this invention. Inquiries concerning rights for its commercial use should be addressed to*

*Intellectual Property group*

*JPL*

*Mail Stop 202-233*

*4800 Oak Grove Drive*

*Pasadena, CA 91109*

*(818) 354-2240*

*Refer to NPO-21173, volume and number of this NASA Tech Briefs issue, and the page number.*

## Multilayer Patch Antenna Surrounded by a Metallic Wall

This antenna provides a gain of about 14 dB.

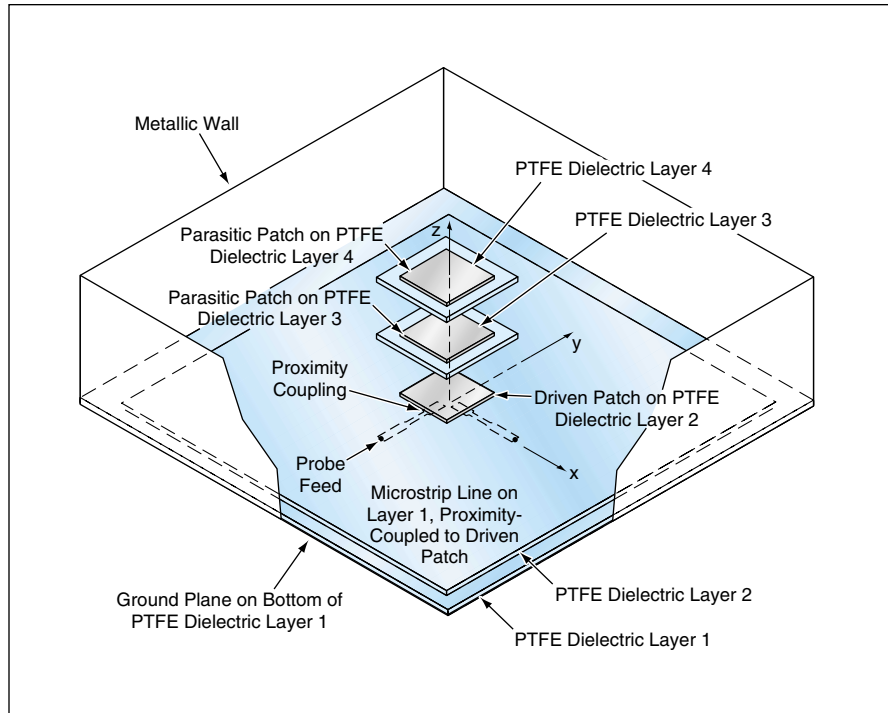
NASA's Jet Propulsion Laboratory, Pasadena, California

A multilayer patch antenna, similar to a Yagi antenna, surrounded by a metallic wall has been devised to satisfy requirements to fit within a specified size and shape and to generate a beam with a half-power angular width of  $\leq 40^\circ$ . This antenna provides a gain of about 14 dB; in contrast, the gain of a typical single-patch antenna lies between 5 and 6 dB.

This antenna can be considered an alternative to a two-dimensional array of patch antenna elements, or to a horn or helical antenna. Unlike a two-dimensional array of patches, this antenna can function without need for a power-division network (unless circular polarization is needed). The profile of this antenna is lower than that of a horn or a helical antenna designed for the same frequency. The primary disadvantage of this antenna, relative to a horn or a helical antenna, is that its footprint is slightly larger.

This antenna (see figure) includes four dielectric substrate layers of polytetrafluoroethylene (PTFE) [which has a relative permittivity of 2.2], on which metallic patch antenna elements are formed. It also includes two thick spacer layers of a foam that has a relative permittivity of 1.08. A metallic wall surrounds the aforementioned components on four sides, forming an open cavity suggestive of a shallow, boxlike feed horn. The length of each side is about two wavelengths and the total height is about one wavelength. Without this cavity, the antenna gain achieved was 2 dB lower.

A microstrip feed line is etched on the upper side of PTFE dielectric layer 1 and is proximity-coupled to a driven patch element located on the upper side of PTFE dielectric layer 2. A ground plane is lo-



This Multilayer Patch Antenna protrudes less than does a horn or a helical antenna. For clarity, the layers of foam that support PTFE dielectric layers 3 and 4 are not shown in this view.

cated on the bottom of PTFE dielectric layer 1 and is electrically connected to the metallic wall. The foam layers support PTFE dielectric layers 3 and 4, on which are located two additional patches that function as "parasitic" antenna elements in that they are electromagnetically coupled to the driven element.

The use of proximity coupling by a microstrip feed line assists mainly in matching to the high input impedance attributable to the three-layer configuration of patch antenna elements. Some fine tuning of the proximity coupling is effected by widening of the microstrip

under the driven patch. By enabling the driven patch to exist on a substrate thicker than that of the microstrip feed line, the proximity coupling likely increases the bandwidth of the antenna moderately. One can provide for circular polarization by introducing a microstrip power divider with a  $90^\circ$  phase delay in the microstrip feed line to one of two proximity couplings.

This work was done by Mark Zawadzki and John Huang of Caltech for NASA's Jet Propulsion Laboratory. Further information is contained in a TSP (see page 1). NPO-21242



## Software To Secure Distributed Propulsion Simulations

**CORBASec brings role-based security to CORBA-object-wrapped simulations.**

*John H. Glenn Research Center, Cleveland, Ohio*

Distributed-object computing systems are presented with many security threats, including network eavesdropping, message tampering, and communications middleware masquerading. NASA Glenn Research Center, and its industry partners, has taken an active role in mitigating the security threats associated with developing and operating their proprietary aerospace propulsion simulations. In particular, they are developing a collaborative Common Object Request Broker Architecture (CORBA) Security (CORBASec) test bed to secure their distributed aerospace propulsion simulations. Glenn has been working with its aerospace propulsion industry partners to deploy the Numerical Propulsion System Simulation (NPSS) object-based technology. NPSS is a program focused on reducing the cost and time in developing aerospace propulsion engines.

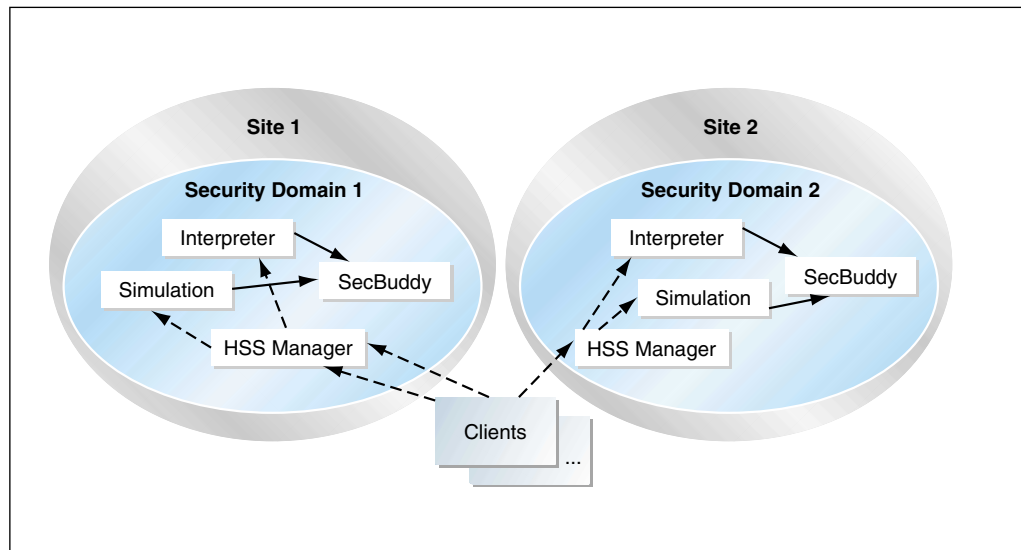
NPSS has been developed by Glenn and sponsored by the NASA Ames Research Center. Glenn is an active domain member of the Object Management Group (OMG) — an open membership, not-for-profit consortium that produces and manages computer industry specifications (i.e., CORBA) for interoperable enterprise applications. When NPSS is deployed, it will assemble a distributed-aerospace propulsion-simulation scenario from proprietary analytical CORBA servers and execute them with security afforded by the CORBASec implementation.

The NPSS CORBASec test bed utilizes the Portable Object Adaptor (POA) architecture from the VisiBroker 4.x Object Request Broker (ORB) [Borland Software Corp., Scotts Valley, CA], and the Orbix 2000 ORB [IONA Technologies, Dublin, Ireland, with U.S. headquarters in Waltham, MA]. Quadraxis [Software Solutions Division of Hitachi

Computer Products (America), Inc., Waltham, MA] integrated both VisiBroker 4.x and Orbix 2000 ORB architectures with their security service [Hitachi Security Service (HSS)]. The NPSS required a security service that was compatible with both ORBs. Glenn and two United States aeropropulsion-industry companies are the initial partners contributing to the NPSS CORBASec test

will take some time before the CORBA and CORBASec vendors implement this standard solution. NPSS chose to move ahead with a workable solution.

The CORBASec architecture is a flexible ORB security architecture that supports both security-unaware and security-aware application development. CORBASec security-unaware security features are primarily configuration-



The **Functional Blocks** and the relationships among them depicted in this diagram represent the CORBASec multiple security domain, multiple ORB interceptor services, and application invoked architecture.

bed. The test bed uses Security SecurID [RSA Security Inc., Bedford, MA] two-factor, token-based authentication together with HSS digital-certificate-based authentication to validate the various NPSS users.

The CORBASec test bed was integrated across firewalls. The process of getting CORBASec to communicate across firewalls was a large accomplishment. Unlike processing Hypertext Transfer Protocol (HTTP) messaging, firewalls do not have designated ports for CORBA Internet Inter-ORB Protocol (IIOP) traffic. NPSS also verified the CORBASec and firewall design by testing with multiple vendors' firewalls. The OMG is now working on a Firewall Traversal specification that promises to provide a standard solution to the CORBASec firewall-integration problem. It

based, requiring very little programming and its security services are implicitly invoked at the ORB interceptor layer. The CORBASec security-unaware architecture spares the application developer from having to write large amounts of security code as the ORB interceptor layer has been configured to handle CORBASec message traffic automatically. The CORBASec security-aware architecture is for applications that need fine-grain security. Security-aware applications enforce fine-grain or application-specific security policies via the CORBASec application programming interface (API) explicitly invoked security services. Unlike security infrastructure-based APIs such as the java.security package, the Java Cryptography Extension (JCE), and the Java Authentication and Authorization Service (JAAS), COR-

BASec [like Enterprise Java Beans (EJB)] supports container-based security, in which a rich array of security services enforce security transparently, allowing the developer to concentrate on building the application rather than the supporting infrastructure. The paradigm shift away from a security API results in security software that is controlled and managed at the ORB interceptor layer and is less prone to programming error.

Within the computer-security discipline there is much talk about role-based security. In the distributed-computer-security world, CORBASec, unlike other distributed role-based security models (e.g., EJB security), defines security domains to allow partitioning of enterprise systems that need to secure large numbers of resources. The NPSS team needed a design suitable for the enterprise systems and therefore, we chose to use the CORBASec approach. The choice of a design that supports multiple security domains has enabled the NPSS team to develop a highly scalable architecture that allows room for growth.

The CORBASec test bed is designed to provide peer (client and server) role-

based authorized security at the CORBA object (interface, method, and variable) levels. For the purposes of discussion, this article focuses on the functionality of the peer client: The CORBASec client authorization architecture (role-based design) allows each client access to a simulation object's functionality based on a run-time comparison of the clients' granted roles and credentials against the required rights of the object. The test bed uses the HSS administration tool to configure three NPSS client user roles: developer, general user, and restricted user. Initially, each client role-based user is checked for the proper security domain access. Developers are granted full access to the private and public simulation object variables and methods as well as access to methods unique to programmers. General users are granted full access to all private and public simulation object variables and methods (except developer-only methods). Restricted users are granted only public access. If necessary, various other role-based configurations can be developed with the CORBASec test bed and its HSS administration tool.

In the figure, the two ovals labeled Site 1 and Site 2 represent separate

aerospace propulsion company network sites. The two ovals labeled Security Domain 1 and Security Domain 2 contain CORBA servers shown as boxes labeled HSS Manager, Interpreter, Simulation, and SecBuddy. The dashed arrows depict the flows of public information among these servers. The solid arrows depict the flows of delegated private information among these servers. The boxes outside the ovals in the figure represent CORBA clients. The HSS Manager at each site authenticates clients for access to specific security domains.

The test bed is expected to demonstrate NPSS CORBASec-specific policy functionality, confirm adequate performance, and validate the required Internet configuration in a distributed collaborative aerospace propulsion environment.

*This work was done by Tammy M. Blaser of Glenn Research Center. Further information is contained in a TSP (see page 1).*

*Inquiries concerning rights for the commercial use of this invention should be addressed to NASA Glenn Research Center, Commercial Technology Office, Attn: Steve Fedor, Mail Stop 4-8, 21000 Brookpark Road, Cleveland Ohio 44135. Refer to LEW-17214.*



## Explicit Pore Pressure Material Model in Carbon-Cloth Phenolic

The explicit model predicts some quantities that a prior implicit model cannot.

Marshall Space Flight Center, Alabama

An explicit material model that uses predicted pressure in the pores of a carbon-cloth phenolic (CCP) composite has been developed. This model is intended to be used within a finite-element model to predict phenomena specific to CCP components of solid-fuel-rocket nozzles subjected to high operating temperatures and to mechanical stresses that can be great enough to cause structural failures. Phenomena that can be predicted with the help of this model include failures of specimens in restrained-thermal-growth (RTG) tests, pocketing erosion, and ply lifting.

Heretofore, an implicit formulation has been used to model the pore pressure. The differences between explicit and implicit models can be illustrated with the theoretical solution for stress and strain in an RTG test. The equations for the explicit case are:

$$\begin{aligned}\sigma_x &= -\alpha_x E_x \Delta T + (2\nu_{xw} - 1)\sigma_p, \\ \epsilon_\theta &= (\alpha_w + \nu_{xw}\alpha_x)\Delta T + (1 - 2\nu_{xw}\nu_{wx} - \nu_{wf})\sigma_p/E_w, \text{ and} \\ \sigma_w &= \sigma_f = \sigma_p\end{aligned}$$

where

$\sigma_x$  is the measured axial stress,

$\epsilon_\theta$  is the measured lateral (circumferential) strain,

$\sigma_w$  is the warp stress,

$\sigma_f$  is the fill stress,

$\sigma_p$  is the pore stress,

$\alpha_x$  is the across-ply coefficient of thermal expansion (CTE),

$\alpha_w$  is the warp CTE,

$\Delta T$  is the change in temperature,

$E_x$  is the across-ply modulus of elasticity,

$E_w$  is the warp modulus of elasticity,

$\nu_{xw}$  is the (across-ply)-warp Poisson's ratio,

$\nu_{wx}$  is the warp-(across-ply) Poisson's ratio, and

$\nu_{wf}$  is the warp-fill Poisson's ratio.

For the implicit case, the  $\sigma_p$  term is zero. The most obvious implication of

this is that the fiber stresses ( $\sigma_w$ ,  $\sigma_f$ ) would also be zero for an implicit material model. At the same time, fiber failure is known to occur during RTG testing. Thus, the failure of RTG specimens cannot be predicted with an implicit material model, but can with an explicit model.

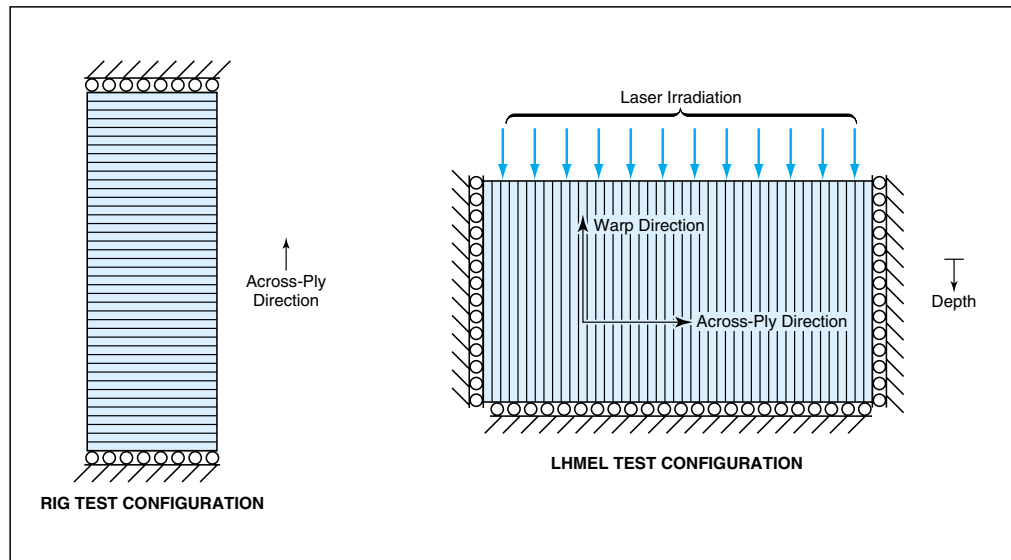
One aspect of the development of the explicit model was to ensure that the properties used in the equations came from tests performed at low heating rates, so that effects of pore pressure could be considered separately from other effects. Another aspect of the development of the explicit model is the use of an additional equation for the pore stress:

$$\sigma_p = P_p \eta,$$

where  $P_p$  is the pore pressure and  $\eta$  is the porosity of the CCP material. Here, the pore stress is regarded as the stress induced in the structure by the pore pressure. Because  $P_p$  had not been measured in an RTG configuration, for the purpose of testing and comparison, a pore-stress distribution versus tempera-

ture was assumed, then modified to correlate with measured RTG data. The only information known about the pore stress was that many RTG specimens had exhibited fiber failure at temperatures from 750 to 900 °F (399 to 482 °C). Knowing that the fiber stress equals the pore stress and the fiber tensile capability in this temperature range, it is possible to calculate a pore-stress data point.

The explicit and implicit models were compared in analyses of data from (1) RTG tests (2) high-heating-rate tests of a different type called "LHMEL" because they were performed in a facility called the "Laser Hardened Materials Evaluation Laboratory." The figure depicts the basic RTG and LHMEL configurations. Both models were found to be equally capable of predicting the axial stresses and lateral strains measured in the RTG tests. The explicit model was found to surpass the implicit one by being able to predict a reasonable fiber stress. On the basis of fiber stress, the explicit model can predict failures of RTG specimens.



An RTG Test is performed on a cylindrical specimen made of plies stacked along the axis and heated uniformly. The axial load and lateral strain are recorded versus temperature. A LHMEL test is performed on 1.5-by-1.5-by-0.75-in. (3.8-by-3.8-by-1.9-cm) specimen that is restrained on all sides except one, which is irradiated with a laser beam at a heating rate equivalent to that in an operating rocket nozzle. The temperature and pore pressure are measured at various distances from the irradiated surface.

Both models were also found to predict similar results for most quantities analyzed with respect to the LHMEI tests. The explicit model was found to surpass the implicit one by being able to predict reasonable mechanical strain and stress in the warp direction. This ability leads to the prediction of pocketing erosion in LHMEI tests. Moreover, the explicit model can also be used to indicate the depth, temperature, and time of occurrence of a pocket.

The analyses revealed that the predictions of the implicit and explicit models are similar except in the cases of certain stress and strain components associated with free expansion under a thermal load. For prediction by the explicit model, these stress components have been shown to be useful for predicting material failures of a CCP used in a solid-fuel rocket motor. Such failures cannot be predicted as easily, if at all, by use of the implicit model. The only major dis-

advantage of the explicit model is that in order to use it, one must have accurate values of pore pressure, data from low-heating-rate tests, and porosity; standard procedures for measuring these quantities have not yet been established.

*This work was done by Danton Gutierrez-Lemini and Curt Ehle of Thiokol Corp., Inc., for Marshall Space Flight Center. Further information is contained in a TSP (see page 1).  
MFS-31501*

## Meshed-Pumpkin Super-Pressure Balloon Design

### Masses of long-life, high-altitude balloons could be decreased substantially.

*NASA's Jet Propulsion Laboratory, Pasadena, California*

An improved, lightweight design has been proposed for super-pressure balloons used to carry scientific instruments at high altitudes in the atmosphere of Earth for times as long as 100 days. [A super-pressure balloon is one in which the pressure of the buoyant gas (typically, helium) is kept somewhat above ambient pressure in order to maintain approximately constant density and thereby regulate the altitude.] The proposed design, called "meshed pumpkin," incorporates the basic concept of the pumpkin design, which is so named because of its appearance (see figure). The pumpkin design entails less weight than does a spherical design, and the meshed-pumpkin design would reduce weight further.

The basic idea of the meshed-pumpkin design is to reinforce the membrane of a pumpkin balloon by attaching a strong, lightweight fabric mesh to its outer surface. The reinforcement would make it possible to reduce the membrane mass to one-third or less of that of the basic pumpkin design while retaining sufficient strength to enable the balloon to remain at approximately constant altitude for months.

For example, the pumpkin balloon shown in the figure is made from a complex composite of polyester fabric, adhesive, polyethylene terephthalate film, and polyethylene film. The balloon has an areal mass density of 62 g/m<sup>2</sup> and a total mass of 2,800 kg. The balloon can carry a payload of 1,600 kg at an altitude of 33 km. One corresponding meshed-pumpkin design calls for reinforcement of the membrane with a 1-by-1-in. (2.54-by-2.54-cm) mesh of polybenzoxazole



This **Pumpkin Balloon** weighs less than a spherical balloon of equal payload capacity. The corresponding meshed pumpkin balloon would have only a fraction of the weight of a pumpkin balloon.

scrim fiber of 25 denier (a lineal mass density of about 2.8 mg/m). With this reinforcement, the complex composite membrane could be replaced by a simple polyethylene film 0.5 mil (12.7 μm) thick, reducing the mass of the balloon to <400 kg. The mesh would provide a strength of 400 N/m, giving a factor of safety of 5, relative to the strength required for a pumpkin balloon with a bulge radius of 8 m.

*This work was done by Jack Jones and Andre Yavrouian of Caltech for NASA's Jet Propulsion Laboratory. Further information is contained in a TSP (see page 1).*

*In accordance with Public Law 96-517, the contractor has elected to retain title to this invention. Inquiries concerning rights for its commercial use should be addressed to Intellectual Property group*

*JPL  
Mail Stop 202-233  
4800 Oak Grove Drive  
Pasadena, CA 91109  
(818) 354-2240*

*Refer to NPO-21139, volume and number of this NASA Tech Briefs issue, and the page number.*

## Corrosion Inhibitors as Penetrant Dyes for Radiography

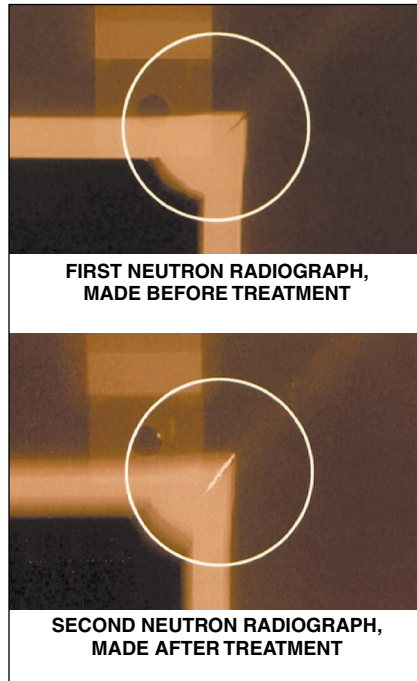
These substances now have dual uses.

Marshall Space Flight Center, Alabama

Liquid/vapor-phase corrosion inhibitors (LVCI) have been found to be additionally useful as penetrant dyes for neutron radiography (and perhaps also x-radiography). Enhancement of radiographic contrasts by use of LVCI can reveal cracks, corrosion, and other defects that may be undetectable by ultrasonic inspection, that are hidden from direct optical inspection, and/or that are difficult or impossible to detect in radiographs made without dyes.

The figure presents two neutron radiographs of part of a frame made of 2219 aluminum alloy. The first radiograph, made before treating the frame with an LVCI, shows some corrosion and includes a faint dark line indicative of a weld crack at a corner. In the second radiograph, made after treating the frame with an LVCI, the weld crack is more clearly visible as a longer, thicker, brighter line.

It has been conjectured that LVCI may be useful as penetrant dyes for x-ray as well



A Weld Crack Is More Clearly Visible in a neutron radiograph made after treatment with an LVCI.

as for neutron radiography. Further research is needed to determine which formulations of LVCI would be most suitable for dual use as corrosion inhibitors and penetrant dyes for radiography. For example, in formulating an LVCI for a particular application it might be possible to add a small amount of x-ray-attenuating material to enhance x-radiographic contrast.

This work was done by Howard L. Novak and Phillip B. Hall of USBI Co. for Marshall Space Flight Center. Further information is contained in a TSP (see page 1).

This invention is owned by NASA, and a patent application has been filed. For further information, contact Sammy Nabors, MSFC Commercialization Assistance Lead, at (256) 544-5226 or sammy.nabors@msfc.nasa.gov. Refer to MFS-31562.

## Transparent Metal-Salt-Filled Polymeric Radiation Shields

These shields offer advantages over ones made from lead foil or leaded glass.

Marshall Space Flight Center, Alabama

“COR-RA” (colorless atomic oxygen resistant — radiation shield) is the name of a transparent polymeric material filled with x-ray-absorbing salts of lead, bismuth, cesium, and thorium. COR-RA is suitable for use in shielding personnel against bremsstrahlung radiation from electron-beam welding and industrial and medical x-ray equipment. In comparison with lead-foil and leaded-glass shields that give equivalent protection against x-rays (see table), COR-RA shields are mechanically more durable.

COR-RA absorbs not only x-rays but also neutrons and  $\gamma$  rays without adverse effects on optical or mechanical performance. The formulation of COR-RA with the most favorable mechanical-durability and optical properties contains 22 weight percent of bismuth to absorb x-rays, plus 45 atomic percent hydrogen for shielding against neutrons.

	Lead	Leaded Glass	COR-RA
<b>Thickness</b>	0.3 mm	1.2 mm	4.5 mm
<b>Areal Mass Density, g/cm<sup>2</sup></b>	0.34	0.75	0.72
<b>Mechanical Quality</b>	Ductile	Brittle	Plastic
<b>Optical Quality</b>	Opaque	Transparent	Transparent
<b>Mass Density</b>	11	6.22	1.6
<b>Use Temperature, °C</b>	<300	<350	<200

The Quantitative and Qualitative Parameters in this table are those of three shields that give equivalent protection against ionizing radiation.

This work was done by David Edwards of Marshall Space Flight Center and John Lennhoff and George Harris of Triton Sys-

tems, Inc. Further information is contained in a TSP (see page 1). MFS-31371



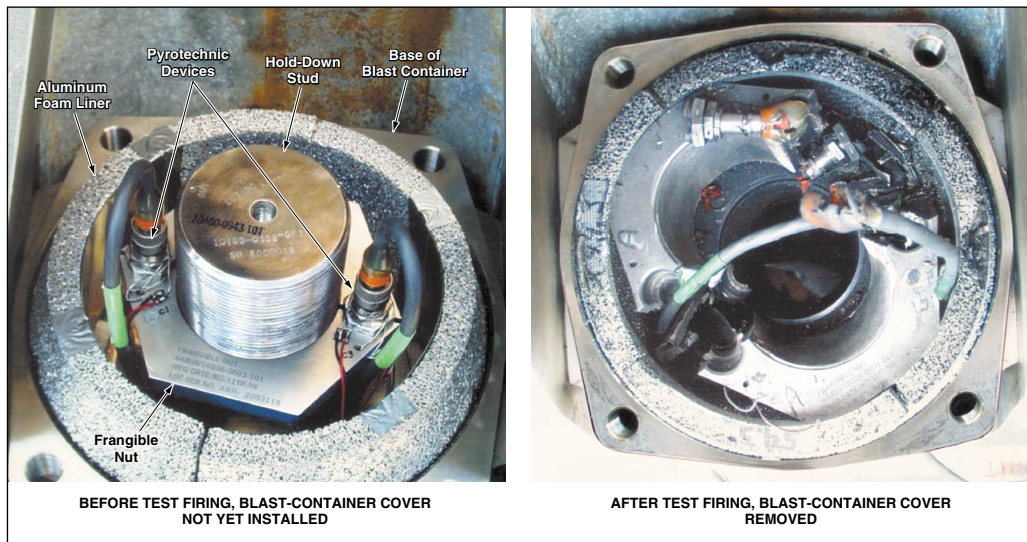
## Lightweight Energy Absorbers for Blast Containers

Aluminum foam liners tested for possible replacement of solid lead liners.

Marshall Space Flight Center, Alabama

Kinetic-energy-absorbing liners made of aluminum foam have been developed to replace solid lead liners in blast containers on the aft skirt of the solid rocket booster of the space shuttle. The blast containers are used to safely trap the debris from small explosions that are initiated at liftoff to sever frangible nuts on hold-down studs that secure the spacecraft to a mobile launch platform until liftoff.

The desire to replace the lead liners arose from the large mass density of lead and its poor energy-absorption performance in the specific application, along with the toxicity of lead and its susceptibility to corrosion in the sea-coast launch environment. The aluminum foam liners are products of a program of design and testing in which the mechanical properties of the foam were tailored for the specific application. Factors considered in the program included mass density, degree of porosity, sizes of pores, resistance to corrosion, strength-to-weight ratio, responses to loads, and variable stress-vs.-strain characteristics.



An Aluminum Foam Liner dissipated the kinetic energy of the debris of a frangible nut and pyrotechnic devices in a test firing in a blast container.

Static drop tests were performed on foams of various thicknesses and densities to optimize the design. On the basis of the results of these tests, aluminum foam liners with densities of 16 and 24 percent were selected. Sample foam liners were tested in a simulated launch configuration (see figure). The results of the tests showed that suitably designed and fabricated aluminum foam liners absorb energy more effectively than the solid lead liners do.

*This work was done by Donald L. Balles, Thomas M. Ingram, Howard L. Novak, and Albert F. Schricker of USBI Co. for Marshall Space Flight Center. Further information is contained in a TSP (see page 1).*

*Inquiries concerning rights for the commercial use of this invention should be addressed to the Patent Counsel, Marshall Space Flight Center; (256) 544-0021. Refer to MFS-31563.*

## Brush-Wheel Samplers for Planetary Exploration

NASA's Jet Propulsion Laboratory, Pasadena, California

A report proposes brush-wheel mechanisms for acquiring samples of soils from remote planets. In simplest terms, such a mechanism would contain brush wheels that would be counter-rotated at relatively high speed. The mechanism would be lowered to the ground from a spacecraft or other exploratory vehicle. Upon contact with the ground, the counterrotating brush wheels would kick soil up into a collection chamber. Thus, in form and function, the mecha-

nism would partly resemble traditional street and carpet sweepers. The main advantage of using of brush wheels (in contradistinction to cutting wheels or other, more complex mechanisms) is that upon encountering soil harder than expected, the brushes could simply deflect and the motor(s) could continue to turn. That is, sufficiently flexible brushes would afford resistance to jamming and to overloading of the motors used to rotate the brushes, and so

the motors could be made correspondingly lighter and less power hungry. Of course, one could select the brush stiffnesses and motor torques and speeds for greatest effectiveness in sampling soil of a specific anticipated degree of hardness.

*This work was done by Tommaso Rivellini of Caltech for NASA's Jet Propulsion Laboratory. Further information is contained in a TSP (see page 1). NPO-30665*



## ■ Dry Process for Making Polyimide/Carbon-and-Boron-Fiber Tape

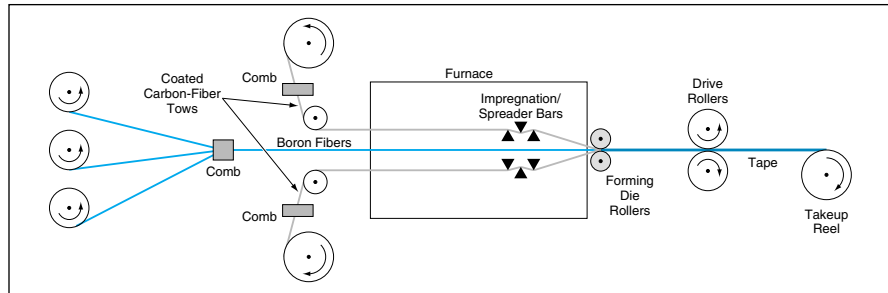
The tape has superior properties and can be used in automated tape placement.

Langley Research Center, Hampton, Virginia

A dry process has been invented as an improved means of manufacturing composite prepreg tapes that consist of high-temperature thermoplastic polyimide resin matrices reinforced with carbon and boron fibers. Such tapes are used (especially in the aircraft industry) to fabricate strong, lightweight composite-material structural components. The inclusion of boron fibers results in compression strengths greater than can be achieved by use of carbon fibers alone.

Until now, polyimide/carbon-and-boron-fiber tapes have been made in a wet process: Boron fibers are calendered onto a wet prepreg tape comprising carbon fibers coated with a polyimide resin in solution. In the calendering step, the boron fibers, which typically have relatively large diameters, are pushed only part way into the wet prepreg. As a result, the boron fibers are not fully encapsulated with resin. In addition, the presence of solvent in the prepreg contributes significantly to the cost of the finished product in two ways: (1) the tackiness and other handling qualities are such that the prepreg tape must be laid up in a labor-intensive process and (2) the solvent must be removed and recovered before and/or during the final cure of the polyimide.

The present dry process is intended to enable the manufacture of prepreg tapes (1) that contain little or no solvent; (2) that have the desired dimensions, fiber areal weight, and resin content; and (3) in which all of the fibers are adequately wetted by resin and the boron fibers are fully encapsulated and evenly dispersed. Prepreg tapes must have these properties to be useable in the manufacture of high-



A Layer of Boron Fibers is formed between two layers of resin-coated carbon-fiber tows. The fibers in each layer are spaced apart in the direction perpendicular to the page. The layers are heated and pressed together to form a composite tape.

quality composites by automated tape placement. The elimination of solvent and the use of automated tape placement would reduce the overall costs of manufacturing.

In this process, a layer of parallel boron fibers is formed and sandwiched between two layers of parallel carbon-fiber tows coated with a powdered polyimide resin. The layers are then heated and pressed together to form a composite tape. As shown in the figure, the boron fibers and the powder-coated carbon-fiber tows are pulled off reels and through combs that form the groups of fibers into the various layers with the lateral spacings consistent with the desired areal densities of carbon and boron fibers. The three layers are pulled through a furnace and maintained parallel until they reach a position where each layer of coated carbon-fiber tows slides against a set of impregnation/spreader bars. The temperature zones in the furnace are set to provide enough heat to melt the polyimide before arrival at the bars. The bars are heated to promote the flow of the resin system while facilitating

the spreading of the tows as they slide over and under the bars.

After passing the bars, the layers are brought out of the furnace and pressed together between two forming die rollers. The speed of pulling of the tape and its fiber constituents is controlled by means of a pair of drive rollers downstream of the forming die rollers. The speed is chosen such that the time at temperature is adequate for the required melt flow. After passing through the drive rollers, the finished tape is wound on a takeup reel.

*This work was done by Harry L. Belvin, Roberto J. Cano, and Norman J. Johnston of Langley Research Center and Joseph M. Marchello of Old Dominion University. Further information is contained in a TSP (see page 1).*

*This invention has been patented by NASA (U.S. Patent No. 6,500,370). Inquiries concerning nonexclusive or exclusive license for its commercial development should be addressed to Barry Price, Technology Commercialization Program Office, Langley Research Center, MS 200, Hampton, VA 23861; E-mail: b.l.price@larc.nasa.gov. Refer to LAR-15470-1.*

## ■ Relatively Inexpensive Rapid Prototyping of Small Parts

Paper drawings and the associated delays in fabrication are eliminated.

Lyndon B. Johnson Space Center, Houston, Texas

Parts with complex three-dimensional shapes and with dimensions up to 8 by 8 by 10 in. (20.3 by 20.3 by 25.4 cm) can be made as unitary pieces of a room-tempera-

ture-curing polymer, with relatively little investment in time and money, by a process now in use at Johnson Space Center. The process is one of a growing number of

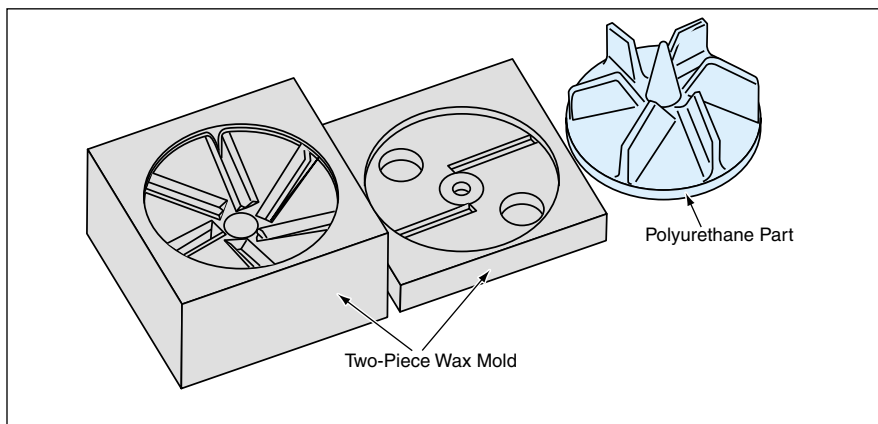
processes and techniques that are known collectively as the art of rapid prototyping. The main advantages of this process over other rapid-prototyping processes are

greater speed and lower cost: There is no need to make paper drawings and take them to a shop for fabrication, and thus no need for the attendant paperwork and organizational delays. Instead, molds for desired parts are made automatically on a machine that is guided by data from a computer-aided design (CAD) system and can reside in an engineering office.

The process centers around the Actua 2100 (or equivalent) office-compatible rapid-prototyping machine. This machine is essentially a three dimensional printer that builds a part directly from a CAD data that specify a solid mathematical model, in the same manner as that of a rapid-prototyping machine of the stereolithographic or fused-deposition-modeling type. A CAD operator merely builds a plot file and submits it to the machine (this submission takes approximately one minute per part), then the machine builds the part. The time that it takes to build the part could be a few hours or as much as 30 hours, depending on the size of the part.

The machine builds parts with extremely fine detail but with two severe drawbacks. One of the drawbacks is that it makes parts of a wax that lacks toughness and strength. The other drawback is that any surfaces that are facing down with respect to the machine are covered with supports. These supports can easily be cleaned off by a light manual brushing, but the resulting surfaces are not smooth.

The present rapid-prototyping process overcomes these drawbacks. The steps of the process are the following:



A **Two-Piece Mold** is used to make a complex three-dimensional part.

1. The CAD system is used to design the desired part.
2. Taking advantage of a solid-modeling subtraction capability, the CAD system is used to design a mold that contains a cavity of the size and shape of the desired part.
3. The CAD model of the mold is sliced into appropriate pieces to eliminate any downward-facing surfaces (to prevent the production of supports on surfaces of the molded part).
4. Filling ports and vents are added to the CAD model to complete the mold design.
5. The data from the CAD model of the mold pieces are submitted as a print job to the rapid-prototyping machine, then the machine builds the mold pieces.
6. The mold pieces are taped together and filled with a room-temperature-curing

polymer. The polymer used by the developer of this method is a durable polyurethane that becomes cured sufficiently for removal from the mold in about 1/2 hour.

7. The mold is removed and, after removal of any minor flashing, the part is ready for use.

One advantage of using a wax as the mold material is that mold can be removed from the part by melting, if necessary (the melting temperature of the wax is less than that of the polyurethane). Of course, if the mold is melted and it is desired to produce more copies of the part, then more copies of the mold must be built from the CAD files.

*This work was done by Scott A. Swan of Johnson Space Center. Further information is contained in a TSP (see page 1). MSC-23035*





## Magnetic Field Would Reduce Electron Backstreaming in Ion Thrusters

Erosion of accelerator grid could also be reduced.

John H. Glenn Research Center, Cleveland, Ohio

The imposition of a magnetic field has been proposed as a means of reducing the electron backstreaming problem in ion thrusters.

Electron backstreaming refers to the backflow of electrons into the ion thruster. Backstreaming electrons are accelerated by the large potential difference that exists between the ion-thruster acceleration electrodes, which otherwise accelerates positive ions out of the engine to develop thrust. The energetic beam formed by the backstreaming electrons can damage the discharge cathode, as well as other discharge surfaces upstream of the acceleration electrodes. The electron-backstreaming condition occurs when the center potential of the ion accelerator grid is no longer sufficiently negative to prevent electron diffusion back into the ion thruster. This typically occurs over extended periods of operation as accelerator-grid apertures enlarge due to erosion. As a result, ion thrusters are required to operate at increasingly negative accelerator-grid voltages in order to prevent electron backstreaming. These larger negative

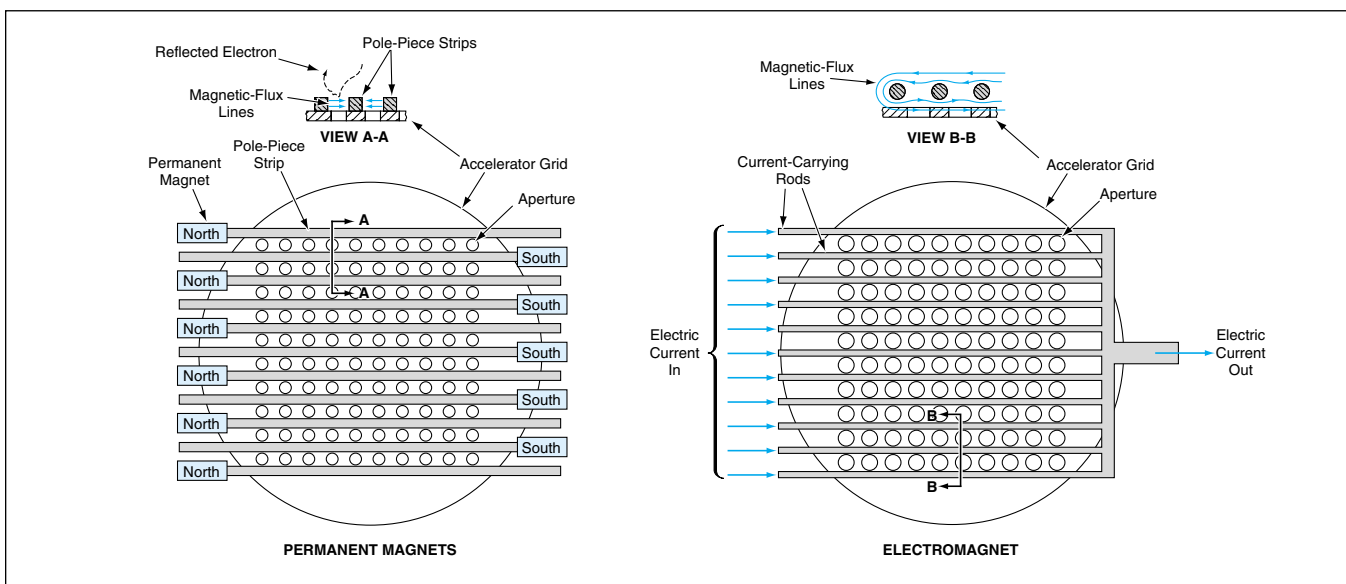
voltages give rise to higher accelerator-grid erosion rates, which in turn accelerates aperture enlargement. Electron backstreaming due to accelerator-grid-hole enlargement has been identified as a failure mechanism that will limit ion-thruster service lifetime.

The proposed method would make it possible to not only reduce the electron backstreaming current at and below the backstreaming voltage limit, but also reduce the backstreaming voltage limit itself. This reduction in the voltage at which electron backstreaming occurs provides operating margin and thereby reduces the magnitude of negative voltage that must be placed on the accelerator grid. Such a reduction reduces accelerator-grid erosion rates. The basic idea behind the proposed method is to impose a spatially uniform magnetic field downstream of the accelerator electrode that is oriented transverse to the thruster axis. The magnetic field must be sufficiently strong to impede backstreaming electrons, but not so strong as to significantly perturb ion trajectories.

An electromagnet or permanent magnetic circuit can be used to impose the transverse magnetic field downstream of the accelerator-grid electrode. For example, in the case of an accelerator grid containing straight, parallel rows of apertures, one can apply nearly uniform magnetic fields across all the apertures by the use of permanent magnets of alternating polarity connected to pole pieces laid out parallel to the rows, as shown in the left part of the figure. For low-temperature operation, the pole pieces can be replaced with bar magnets of alternating polarity. Alternatively, for the same accelerator grid, one could use an electromagnet in the form of current-carrying rods laid out parallel to the rows, as shown in the right part of the figure.

*This work was done by John E. Foster of Glenn Research Center. Further information is contained in a TSP (see page 1).*

*Inquiries concerning rights for the commercial use of this invention should be addressed to NASA Glenn Research Center, Commercial Technology Office, Attn: Steve Fedor, Mail Stop 4-8, 21000 Brookpark Road, Cleveland, Ohio 44135. Refer to LEW-17174.*



Either Permanent Magnets or an Electromagnet could be used to apply magnetic fields across the apertures in an ion-accelerator grid. The fields would be made strong enough to reduce backstreaming of electrons without significantly perturbing ion trajectories. In the permanent-magnet case, some external magnetic-circuit components (yokes and opposite poles of permanent magnets) are omitted from the drawing for the sake of simplicity.

# Alternative Electrochemical Systems for Ozonation of Water

Hydrogen gas, ozone gas, and ozonated water can be delivered under pressure.

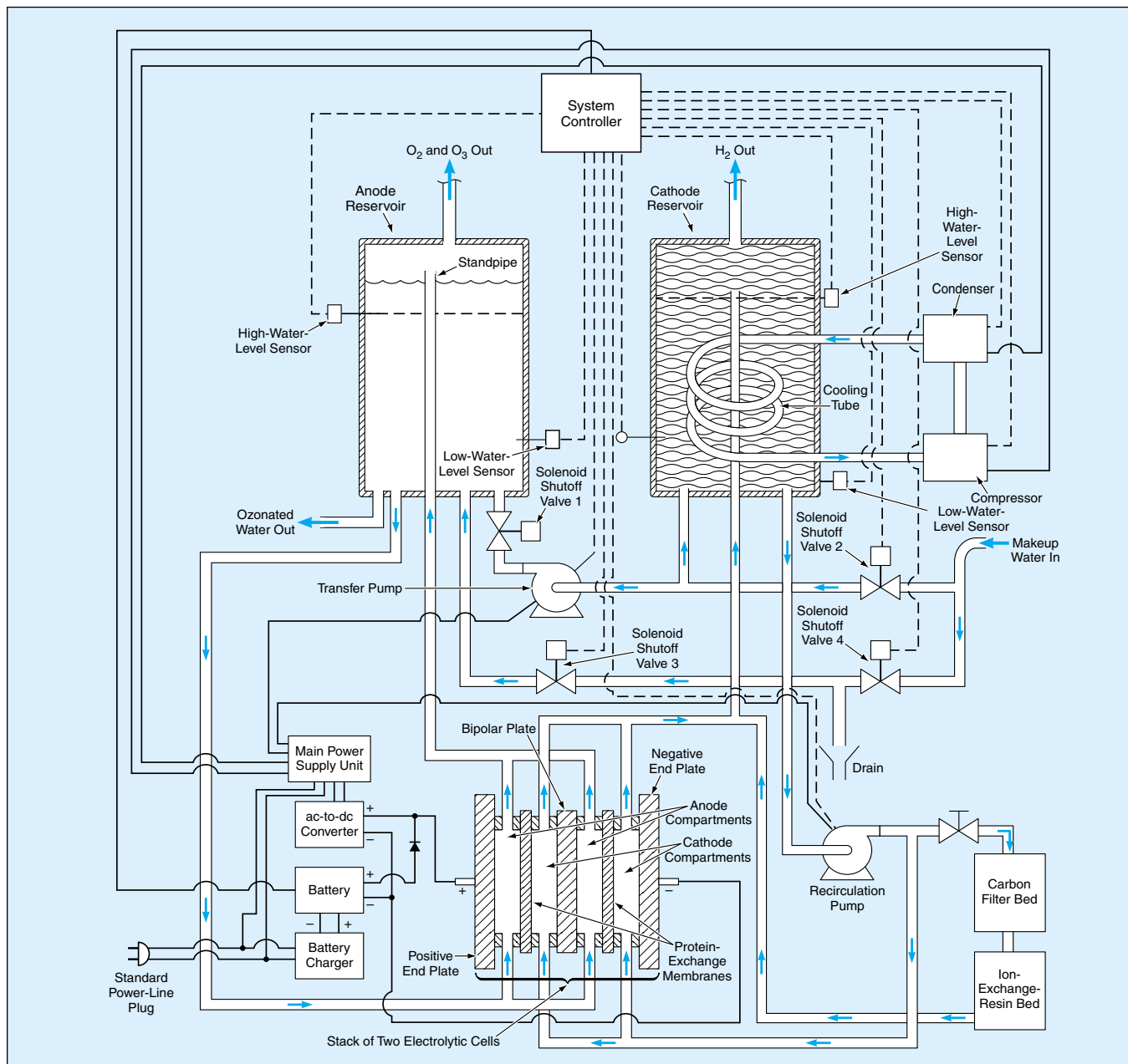
Lyndon B. Johnson Space Center, Houston, Texas

Electrochemical systems that are especially well suited for the small-scale generation of ozone and ozonated water for local use have been invented. These systems can operate with very little maintenance, and the only inputs needed during operation are electric power and water. These systems are closely related to the ones described in "Electrochemical Systems Generate Ozone and

Ozonated Water" (MSC-23046), NASA Tech Briefs, Vol. 26, No. 3 (March 2002), page 68. Ozonated water produced by these systems can be used in diverse industrial applications: A few examples include sterilization in the brewing industry, general disinfection, and treatment of sewage and recycled water.

The basic principle of operation admits of several alternative system configurations, of which one is depicted schematically in the figure.

The heart of the system is a stack of electrolytic cells, each containing a proton-exchange membrane (which serves as a solid electrolyte) sandwiched between a catalytic anode and a catalytic cathode. Preferably, the proton-exchange membrane is made of a perfluorinated sulfonic acid polymer. During electrolysis, a mixture



This System Generates Ozonated Water, with an  $O_2/O_3$  gas mixture and  $H_2$  gas as by-products. The water pressure is high enough and the water temperature low enough to maintain an adequate concentration of dissolved ozone for a usefully long time.

of  $O_2$  and  $O_3$  gases is generated at the anode and  $H_2$  is generated at the cathode. Some of the  $O_3$  generated at the anode becomes dissolved in the water. The proportion of  $O_3$  in the  $O_2/O_3$  mixture can be maximized by the selection of suitable electrode materials and the use of a high overpotential. Although the proton-exchange membrane conducts protons, it does not conduct electrons. It is also impermeable by gases; consequently, it maintains separation between the  $O_2/O_3$  mixture evolved at the anode and the  $H_2$  evolved at the cathode.

Water circulates upward through the anode and cathode compartments of the stack of electrolytic cells. Water from the bottom of an anode and a cathode reservoir is gravity-fed to the bottom inlet of the anode and cathode compartment, respectively. From the tops of the anode compartments, the mixture of water and  $O_2$  and  $O_3$  gases and water containing dissolved ozone can flow freely upward, through a standpipe that ends in the anode reservoir, and from the tops of the cathode compartments, the mixture of water and  $H_2$  gas can flow freely upward, through standpipe that ends in the cathode reservoir. The reservoirs double as liquid/gas separators:  $O_2$  and  $O_3$  diffuse out of the water in the anode reservoir,

are collected at the top of the reservoir, and are either vented or sent to an ozone-consuming process. Similarly,  $H_2$  diffuses out of the water in the cathode reservoir, is collected at the top of that reservoir, and can be flared, vented, or sent to an  $H_2$ -consuming process.

As water is consumed in electrolysis and/or withdrawn from the anode reservoir for external use, makeup water (which must be deionized) is supplied to the system. The addition of makeup water and the circulation of water between the anode and cathode plumbing subsystems is controlled to maintain the desired levels of water in the reservoirs. The control subsystem responds to measurements by high- and low-water-level sensors in the reservoirs and exerts control via several solenoid shutoff valves and a transfer pump. The makeup water can be potable water, in which case it is preferable to introduce a secondary recirculation loop that purifies the water circulated through the cathode compartments and reservoir. Typically, such a recirculation loop includes a recirculation pump in series with a carbon-filter bed followed by an ion-exchange-resin bed.

The system operates with pressures high enough to maintain desired high concentrations of dissolved ozone: The

reservoirs and electrolytic cells are preferably designed to operate at gauge pressures up to about 30 psi ( $\approx 0.2$  MPa). Makeup water is conveniently supplied at a gauge pressure of about 50 psi ( $\approx 0.35$  MPa): the supply pressure must exceed the reservoir pressure in order to make the water flow into the reservoirs.

A refrigeration subsystem includes a compressor, a condenser, and a cooling tube coiled within the cathode reservoir. This subsystem removes the heat introduced by electrolysis and maintains the water in the system at or below a set temperature, which is typically about  $35^\circ\text{C}$ : This is an important function because lowering the temperature extends the lifetime of the ozone dissolved in the water.

*This work was done by Craig C. Andrews and Oliver J. Murphy of Lynntech, Inc., for Johnson Space Center.*

*In accordance with Public Law 96-517, the contractor has elected to retain title to this invention. Inquiries concerning rights for its commercial use should be addressed to*

*Lynntech, Inc.*

*3900 Texas Ave. South*

*Suite 106*

*College Station, TX 77845*

*Refer to MSC-23045, volume and number of this NASA Tech Briefs issue, and the page number.*

## Interferometer for Measuring Displacement to Within 20 pm

**Errors are reduced by suppressing effects of polarization leakage and thermal expansion.**

*NASA's Jet Propulsion Laboratory, Pasadena, California*

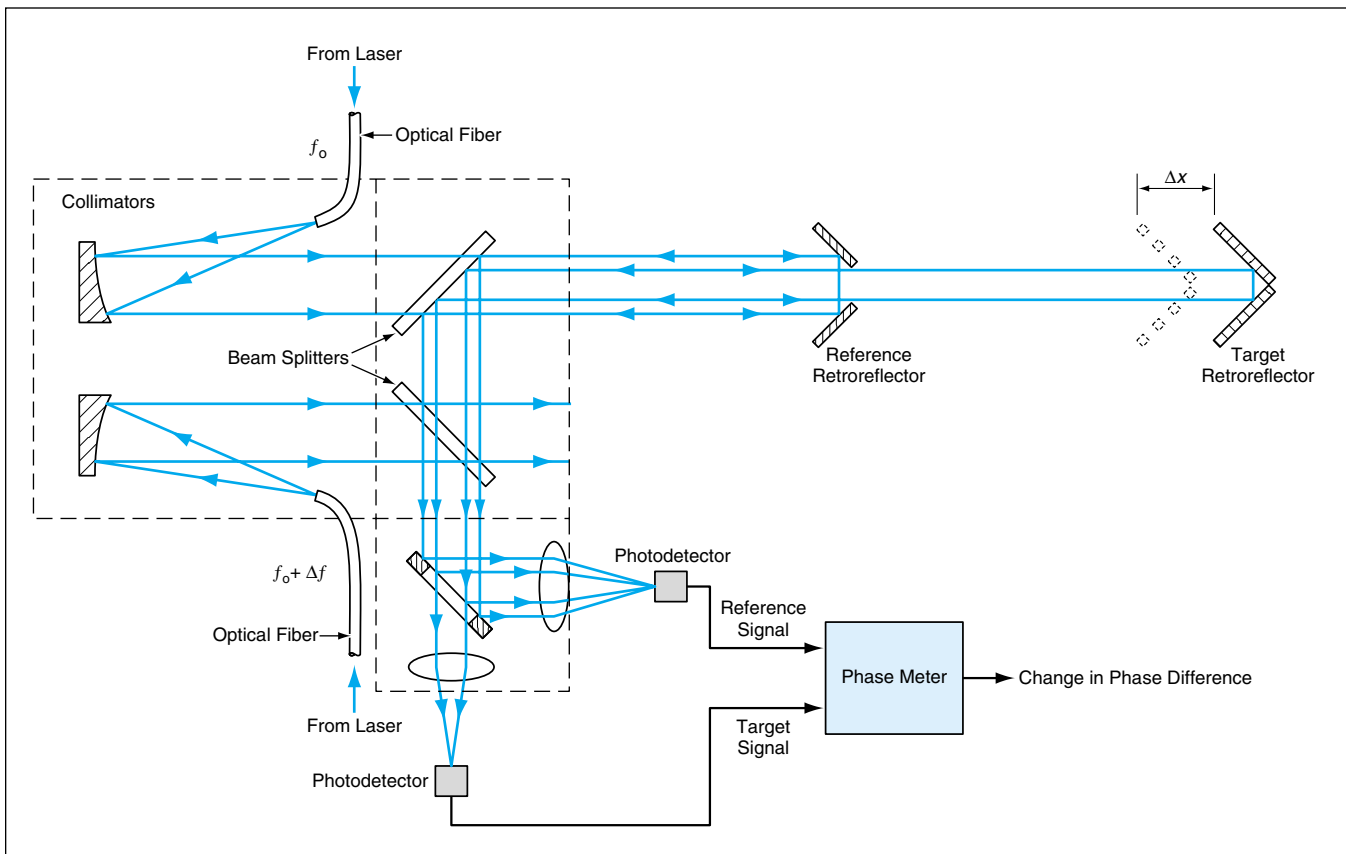
An optical heterodyne interferometer that can be used to measure linear displacements with an error  $\leq 20$  pm has been developed. The remarkable accuracy of this interferometer is achieved through a design that includes (1) a wavefront split that reduces (relative to amplitude splits used in other interferometers) self interference and (2) a common-optical-path configuration that affords common-mode cancellation of the interference effects of thermal-expansion changes in optical-path lengths.

The most popular method of displacement-measuring interferometry involves two beams, the polarizations of which are meant to be kept orthogonal upstream of the final interference location, where the difference between the phases of the two beams is measured. Polarization leakages (deviations from the

desired perfect orthogonality) contaminate the phase measurement with periodic nonlinear errors. In commercial interferometers, these phase-measurement errors result in displacement errors in the approximate range of 1 to 10 nm. Moreover, because prior interferometers lack compensation for thermal-expansion changes in optical-path lengths, they are subject to additional displacement errors characterized by a temperature sensitivity of about 100 nm/K. Because the present interferometer does not utilize polarization in the separation and combination of the two interfering beams and because of the common-mode cancellation of thermal-expansion effects, the periodic nonlinear errors and the sensitivity to temperature changes are much smaller than in other interferometers.

The present interferometer (see figure) makes use of two stable, collimated laser beams — one at a frequency of  $f_0$ , the other at the slightly different frequency of  $f_0 + \delta f$ . The  $f_0$  wavefront is split into two or more sections by a retroreflective reference device that could be, for example, a truncated corner-cube reflector or a mirror with holes. The portion of the  $f_0$  wavefront reflected by the reference device serves as reference wavefront. The portion of the  $f_0$  wavefront not reflected by the reference device is directed to a target in the form of a retroreflector. The target is mounted on the object, the displacement of which one seeks to measure relative to the reference device.

The light reflected by the target travels back through the optical system alongside the retroreflected reference light. Along the way, both the target



This **Heterodyne Interferometer** is used to measure the displacement  $\Delta x$ . In addition to the advantages mentioned in the main text, this interferometer contains fewer parts and can be fabricated with looser tolerances, relative to a typical prior interferometer designed for performing the same measurement.

and reference light beams pass through a beam splitter where the  $f_0 + \delta f$  beam is superimposed upon them. Then by use of truncated mirrors and lenses, (1) the target signal and part of the  $f_0 + \delta f$  signal are sent to one photodetector while (2) the reference signal and part of the  $f_0 + \delta f$  signal are sent to another photodetector. The lowest-frequency components of the heterodyne outputs of the two photodetectors are signals of frequency  $\delta f$ , the difference between the phases of

which is proportional to the amount by which the length of the target path exceeds that of the reference path. Any displacement  $\Delta x$ , of the target along the optical path results in a proportional change in this phase difference. Hence, measurement of the phase difference and of any change in the phase difference yields information on the displacement. One can calculate the displacement by use of the equation

$$\Delta x = \lambda \Delta \phi / 4\pi,$$

where  $\lambda$  is the wavelength of the laser

light and  $\Delta \phi$  is the change in the phase difference.

*This work was done by Feng Zhao of Caltech for NASA's Jet Propulsion Laboratory. Further information is contained in a TSP (see page 1).*

*This invention is owned by NASA, and a patent application has been filed. Inquiries concerning nonexclusive or exclusive license for its commercial development should be addressed to the Patent Counsel, NASA Management Office-JPL; (818) 354-7770. Refer to NPO-21221.*

## UV-Enhanced IR Raman System for Identifying Biohazards

### UV pumping would increase IR Raman emissions.

*NASA's Jet Propulsion Laboratory, Pasadena, California*

An instrumentation system that would include an ultraviolet (UV) laser or light-emitting diode, an infrared (IR) laser, and the equivalent of an IR Raman spectrometer has been proposed to enable noncontact identification of hazardous biological agents and chemicals. In prior research, IR Raman scattering had shown promise as a means of such identification, except that the Raman-scattered

light was often found to be too weak to be detected or to enable unambiguous identification in practical applications. The proposed system (see Figure 1) would utilize UV illumination as part of a two-level optical-pumping scheme to intensify the Raman signal sufficiently to enable positive identification.

The UV and IR lasers would share common reflective optics and would il-

luminate a target simultaneously. The spectrum of IR Raman-scattered light emitted by the target would be characteristic of the target material and could therefore be used to identify the material, provided that the Raman signal was strong enough. The Raman-scattered IR light from the target would be collected and directed through a wavelength-dispersive optical element or,

optionally, through a set of narrow-band filters designed to pass only the Raman wavelengths characteristic of the biological agent(s) or chemical(s) of interest. The spectrally dispersed or filtered light would then strike photodetectors, the outputs of which would be processed to obtain the Raman spectrum or equivalent identifying information. The signal-to-noise ratio of the Raman signal, and hence the effective sensitivity for identification, could be increased by pulsing (in contradistinction to steady-state operation) of the lasers in conjunction with synchronous detection (lock-in amplification) of the photodetector outputs, phase locking, and/or chopping of the light impinging on the photodetectors. The UV pulse emission time would envelop the on-time of the IR excitation pulse. Since the two-pulse set could be independently lengthened, thus shortening time delay to the rising edge of the UV pulse, specific enhancements of the signal-to-noise are possible for a given target material. Thus by tuning the pulse durations and timing offsets, optimal separation of the fluorescence background signal from the Raman signal may be achieved.

A brief description of Rayleigh and Raman scattering is prerequisite to a meaningful description of the principle of the two-level optical-pumping scheme that would be exploited in the proposed system to enhance the Raman signal. Most of the IR light incident upon the target would be Rayleigh-scattered: that is, it would be scattered at the same wavelength as that of the incident IR laser beam because most of the vibrating electrons in the target molecules of interest would relax back to their ground states. A small proportion of all incident photons (of the order of one in a million) would be Raman-scattered: This means that they would be scattered at wavelengths slightly greater than that of the incident IR beam because some of the electrons would relax to vibrational states slightly above the ground state.

The pumping scheme is depicted schematically in Figure 2. The UV laser would pump electrons from the ground state to quantum state 1. The IR laser would further pump the electrons from quantum state 1 to quantum state 2. The electrons would then decay from state 2 by Raman and Rayleigh scattering. The instrument would still work if there were no UV laser because there would be a small

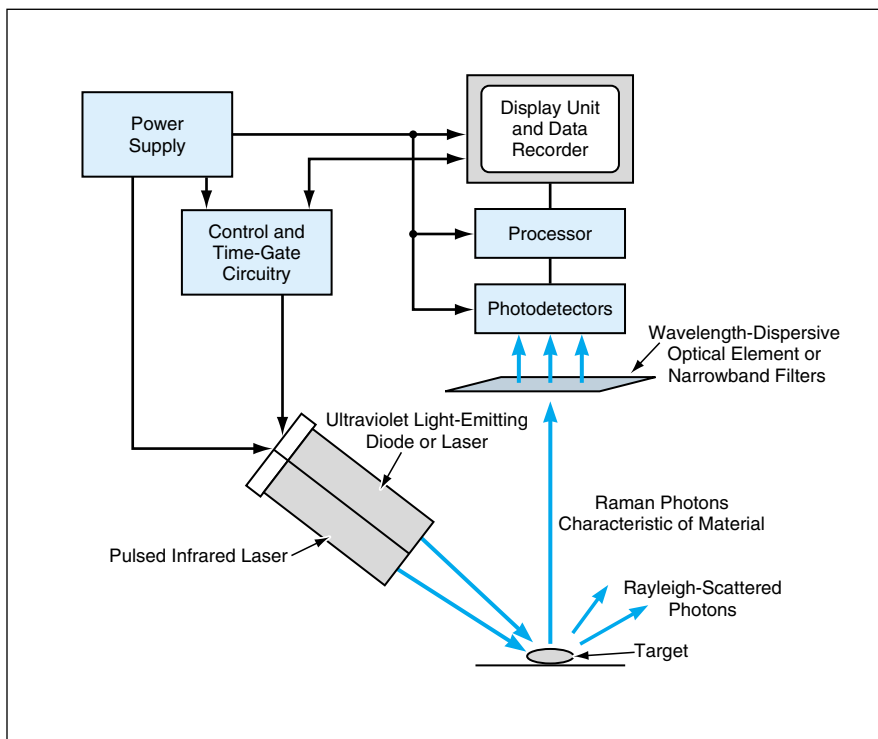


Figure 1. This **Instrumentation System** would induce and measure IR Raman scattering to identify a hazardous material by means of its characteristic Raman-scattering spectrum.

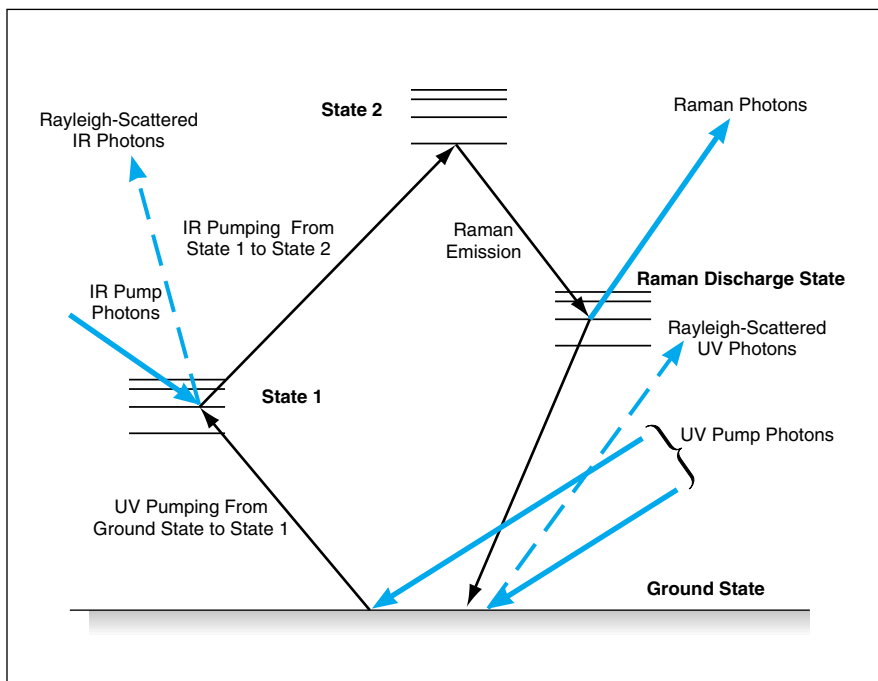


Figure 2. **Two-Level Optical Pumping** by the UV and IR lasers would result in a Raman signal more intense than that obtained by illuminating the target with the IR laser alone.

natural population of electrons in state 1. The role of the UV laser would be simply to increase the population in state 1, thereby making more electrons available for pumping to state 2, thereby further increasing the number of Raman-scattered photons emitted in the decay from state 2.

*This work was done by Robert Stirbl, Philip Moynihan, and Arthur Lane of Caltech for NASA's Jet Propulsion Laboratory. Further information is contained in a TSP (see page 1). NPO-30527*



## Prognostics Methodology for Complex Systems

Automatic method to detect and react to complex degradation and incipient faults.

NASA's Jet Propulsion Laboratory, Pasadena, California

An automatic method to schedule maintenance and repair of complex systems is produced based on a computational structure called the Informed Maintenance Grid (IMG). This method provides solutions to the two fundamental problems in autonomic logistics: (1) unambiguous detection of deterioration or impending loss of function and (2) determination of the time remaining to perform maintenance or other corrective action based upon information from the system. The IMG provides a health determination over the medium-to-long-term operation of the system, from one or more days to years of study. The IMG is especially applicable to spacecraft and both piloted and autonomous aircraft, or industrial control processes.

Condition-Based Maintenance (CBM) has become popular for complex systems due to its cost and reliability advantages

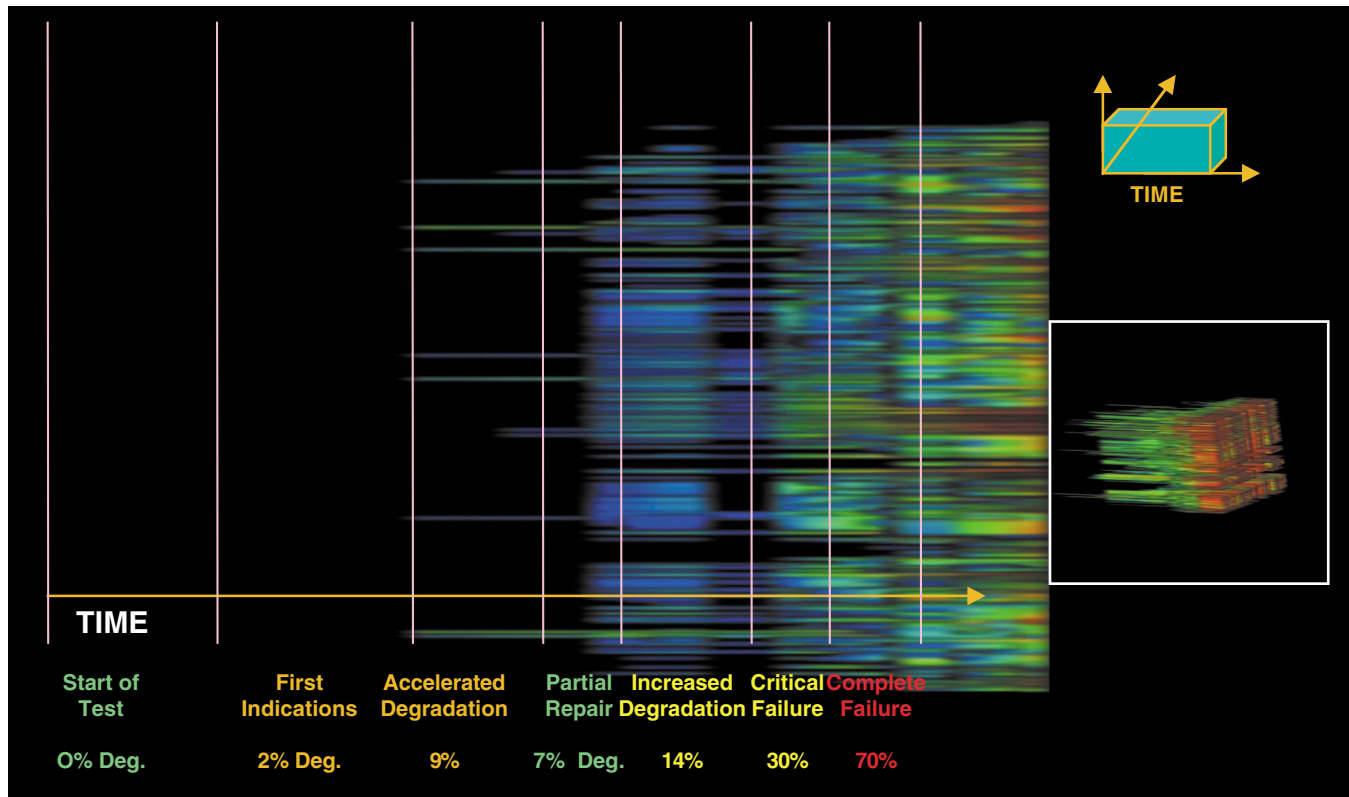
over traditional scheduled maintenance programs. However, CBM is frequently difficult to apply owing to system complexity and the highly stochastic nature of system use and environmental effects. A scalable solution capable of providing a substantial look-ahead capability is required. The IMG method was developed to satisfy this need.

The IMG is based upon a three-dimensional projection, relating successive computations of cross-signal features. The two short axes represent different sensed parameters from the system (typically performance parameters such as temperatures, pressures, etc.), with each pixel representing the coherency between measurements. The third axis represents time, displaying the progression of abnormalities as the system is used.

The IMG is a component of the larger BEAM system ("Beacon-Based Exception Analysis for Multimissions" [NPO-

20827], *NASA Tech Briefs*, Vol. 26, No. 9 (September 2002), page 32). The coherence calculation used in the IMG is derived from the Information State Estimator (ISE) component of BEAM. The ISE computes relationships between large and diverse classes of signals and compares them to an internal statistical model for the purpose of anomaly detection. This notion is extended by the IMG, which combines and normalizes numerous results while providing an operational context.

Graphically, the IMG is represented (see figure) as a color-coded temporal succession of two-dimensional plots, each representing the coherence divergence from the statistical model. From this graphical object, one can easily discern the true functional operability of the system, detect the presence and impact of faults or persistent degradation,



In This Example, the IMG provides a day-to-day assessment of a failing aerospace hydraulic system. Time progresses from left to right on a scale of individual flights. Brighter colors indicate degradation severity, while the density and thickness of lines demonstrates the spread of degradation effects throughout the system. Warning and Failure thresholds as established by existing fault protection are superposed to show the system's sensitivity. Inset: Perspective view of the IMG graphical object.

and assess the effectiveness of repairs or configurational changes. Maintenance recommendations can be derived automatically from this object, providing a continuous evaluation of the need for condition-based maintenance.

The following list outlines the necessary construction steps to apply the IMG:

1. Provide examples of nominal data and partial physics models where possible for purposes of ISE training,
2. Obtain example data of degraded or anomalous performance for training purposes,
3. Compose a listing of preferred maintenance actions to correct faults in

particular components, and

4. Provide a mapping between sensed or manually supplied status variables and system operating mode.

Acceptable operating limits must be established in order to tune prognostic performance for cost effectiveness. These limits must either be set by system experts or “learned” as degradations appear in practice. Like the ISE itself, the IMG is easily upgraded once additional information is available. Limits may also be set using the same thresholds chosen for fault protection.

*This work was done by Sandeep Gulati and Ryan Mackey of Caltech for NASA’s Jet*

**Propulsion Laboratory.** *Further information is contained in a TSP (see page 1).*

*In accordance with Public Law 96-517, the contractor has elected to retain title to this invention. Inquiries concerning rights for its commercial use should be addressed to*

*Intellectual Property group  
JPL*

*Mail Stop 202-233  
4800 Oak Grove Drive  
Pasadena, CA 91109  
(818) 354-2240*

*Refer to NPO-20831, volume and number of this NASA Tech Briefs issue, and the page number.*

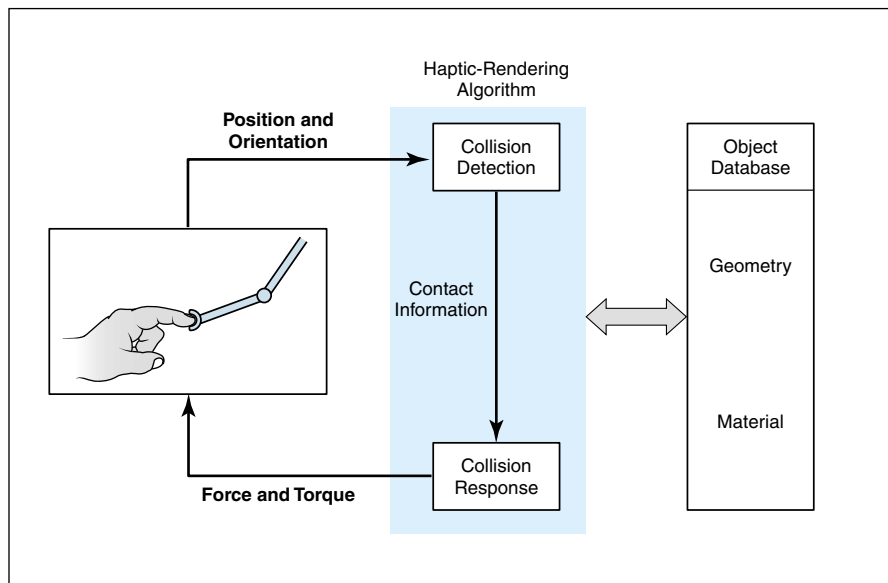
## ➤ Algorithms for Haptic Rendering of 3D Objects

**Tactile displays provide the sensations of touching computationally simulated objects.**

*NASA’s Jet Propulsion Laboratory, Pasadena, California*

Algorithms have been developed to provide haptic rendering of three-dimensional (3D) objects in virtual (that is, computationally simulated) environments. The goal of haptic rendering is to generate tactile displays of the shapes, hardnesses, surface textures, and frictional properties of 3D objects in real time. Haptic rendering is a major element of the emerging field of computer haptics, which invites comparison with computer graphics. We have already seen various applications of computer haptics in the areas of medicine (surgical simulation, telemedicine, haptic user interfaces for blind people, and rehabilitation of patients with neurological disorders), entertainment (3D painting, character animation, morphing, and sculpting), mechanical design (path planning and assembly sequencing), and scientific visualization (geophysical data analysis and molecular manipulation).

Haptic-rendering algorithms enable users to touch, feel, and manipulate 3D objects in virtual environments through force-feedback devices, also known as haptic interfaces. Typically, a haptic-rendering algorithm comprises a collision-detection part and a collision-response part. As the user manipulates the force-feedback device — for example, a fingertip probe as in the figure — the current or recent position and orientation of the probe are acquired and the collision-detection algorithm detects collisions between the fingertip and virtual objects in the vicinity of the fingertip. If a collision is detected, then the collision-response



**A Force-Feedback Device** (in this case, an actuated fingertip probe) commanded by a haptic-rendering algorithm generates a tactual representation of contact between a fingertip and a computationally simulated object.

algorithm computes the forces of interaction between the fingertip and the virtual object(s) and commands the force-feedback device to generate the tactual representation of the object(s). The friction of finger/virtual object contact, the texture of the object, and hardness of the object can be simulated through appropriate spatial and temporal perturbations of the force generated by the force-feedback device. The hardness information for deformable virtual objects can be embodied in geometry- and physics-based mathematical models. So that virtual objects will not feel unnaturally soft, the update rate

of the haptic feedback loop thus described should be at least 1 kHz.

Some elements of the collision-detection algorithms used in computer graphics can be used in computer haptics. For example, haptic-rendering algorithms can easily take advantage of space-partitioning, local-searching, and hierarchical-data-structure techniques of computer graphics to reduce the amount of computation time needed to detect collisions. However, mere detection of collisions as in computer graphics is not enough because how a collision occurs and how it evolves over time are factors that must be



taken into account to compute interaction forces accurately. Going beyond computer-graphics collision-detection algorithms, it is necessary to develop algorithms according to a client-server model to provide for synchronization of visual and haptic displays in order to make update rates acceptably high. For example,

by use of multithreading techniques, one can calculate the contact forces at rate of 1 kHz in one thread while updating visual images at 30 Hz in another thread.

*This work was done by Cagatay Basdogan of Caltech, Chih-Hao Ho of Cambridge Research Associates, and Mandayam Srinivasan of MIT for NASA's Jet Propul-*

*sion Laboratory. Further information is contained in a TSP (see page 1).*

*This software is available for commercial licensing. Please contact Don Hart of the California Institute of Technology at (818) 393-3425. Refer to NPO-21191.*

## Σ Modeling and Control of Aerothermoelastic Effects

**This method makes it possible to design controls to compensate for aerothermoelasticity.**

*Dryden Flight Research Center, Edwards, California*

Aerothermoelasticity comprises those aspects of the dynamics of an aircraft that are caused by flexibility and heating during flight. The concept of aerothermoelasticity is particularly important for hypersonic vehicles that operate at extremely high dynamic pressures. The design requirements for such vehicles often introduce long and thin fuselages subject to elastic bending in low-frequency vibrational modes. Furthermore, surface heating can significantly change the stiffness characteristics of these modes. These aerothermoelastic effects must be considered in the synthesis and analysis of control systems.

A method to include the effects of aerothermoelasticity in designing controls has been developed. Heretofore, large, finite-element mathematical models have typically been used to compute the aerothermoelastic effects; however, these models are not suitable for control engineering. The present method makes it possible to incorporate the results of computational analysis into the small linear models that are typically used in designing controls.

In this method, the procedure to include aerothermoelastic effects in linear models begins with noting the relationship between an effect and a temperature. Essentially, computational studies have indicated the changes in the natural frequencies (that is, frequencies of resonance) and damping parameters of structural vibrational modes that occur at various flight conditions and associated temperatures. In the present method, one simply describes the natural frequency and damping parameter of a linear model as functions of temperature that match the variations observed in the computational studies.

The linear models with associated temperature dependence are described by

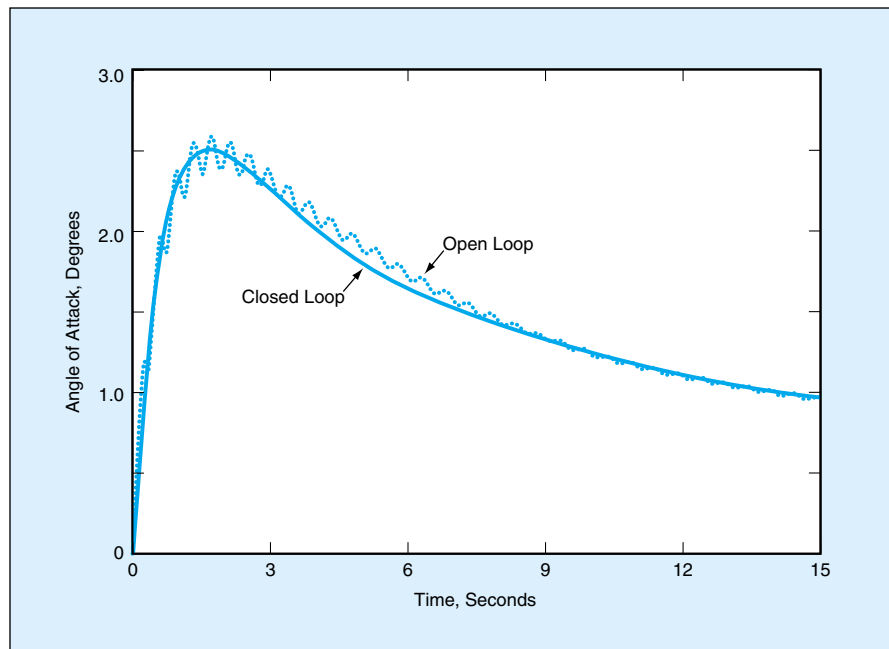
use of a formulation known as linear parameter-varying systems. This formulation enables the efficient description of systems that contain elements that are functions of such time-varying parameters as temperature. Furthermore, there is a set of previously developed theoretical concepts and associated computer programs that enable the design of control systems that incorporate scheduled-gain compensation for dependences on time-varying parameters.

A generic representation of a hypersonic vehicle has been used to demonstrate this method. A range of natural frequencies and damping parameters for the structural dynamics of the vehicle, based on previous computational studies, was assumed. A linear model including representations of the aerothermoelastic ef-

fects was formulated by describing the parameters of the structural dynamics as functions of temperature. A flight controller to actively damp the bending-mode response of this model was designed. The figure shows the open-loop and controlled (closed-loop) responses to an elevator command during a simulated flight with a fast variation of temperature. The open-loop response includes an oscillatory component from the bending mode, whereas the closed-loop response shows that the controller is able to continuously damp this elastic effect despite the time-varying temperature.

*This work was done by Rick Lind of Dryden Flight Research Center. For further information, contact the Dryden Commercial Technology Office at (661) 276-3689.*

*DRC-01-21*



The Responses of a Hypersonic Vehicle to elevator commands were computationally simulated for an open-loop case and for a case of closed-loop control designed according to the present method.

# Processing Digital Imagery To Enhance Perceptions of Realism

Perceptible color and detail are superior to those of other image-enhancement methods.

Langley Research Center, Hampton, Virginia

Multi-scale retinex with color restoration (MSRCR) is a method of processing digital image data based on Edwin Land's retinex (retina + cortex) theory of human color vision. An outgrowth of basic scientific research and its application to NASA's remote-sensing mission, MSRCR is embodied in a general-purpose algorithm that greatly improves the perception of visual realism and the quantity and quality of perceived information in a digitized image. In addition, the MSRCR algorithm includes provisions for automatic corrections to accelerate and facilitate what could otherwise be a tedious image-editing process. The MSRCR algorithm has been, and is expected to continue to be, the basis for development of commercial image-enhancement software designed to extend and refine its capabilities for diverse applications.

Initially, a color image is divided spatially into pixels and, within each pixel, intensity levels are digitized in  $S$  spectral bands. Hence, the initial image data are in the form  $I_i(x,y)$ , where  $x$  and  $y$  are Cartesian pixel coordinates and the subscript  $i$  denotes the  $i$ th spectral band. The MSRCR algorithm begins with the computation of an adjusted value of each  $I_i(x,y)$  in accordance with

$$I_i(x,y)_{\text{adjusted}} = \sum_{n=1}^N w_n \{ \log I_i(x,y) - \log [I_i(x,y) * F_n(x,y)] \}$$

where  $w_n$  is the  $n$ th of  $N$  weighting factors,  $F_n(x,y)$  is the  $n$ th of  $N$  surround functions, and "\*" denotes the convolution operator. Each surround function is uniquely scaled to improve an aspect of the digital image; e.g., dynamic range compression, color constancy, or lightness rendition. The adjusted intensity value for each spectral band at each position is filtered with a common function and then presented to a display device. In the case of a color image, a color-restoration step (essentially, an additional filtering step) is included to make

the image give rise to a human perception of color that closely matches the color perception of a human viewing the original scene depicted in the image.

In the perception of a human viewer, a digital image enhanced by the MSRCR algorithm resembles the original scene, under all kinds and levels of lighting, more closely than does a digital image of the same scene enhanced by any prior known image-data-processing algorithm.

sure that colors in shadowed or brightly illuminated areas are not lost or severely attenuated.

Commercial software, Photoflair for Windows, based on the MSRCR algorithm is now available for use by amateur photographers to optimize brightness and contrast and to enhance detail, and overall sharpness and quality of images. There are numerous other potential applications in medical imaging,



Details in Shadows are more readily perceptible after processing by software based on the MSRCR algorithm.

Other attributes that make the MSRCR algorithm superior to other such algorithms include the following:

- Because all of the desired image-enhancement and -correction functions are performed in a single step, it is much easier for consumers to use software based on the MSRCR algorithm to obtain high-quality digital images. For the same reason, significantly less processing time is needed. No manual manipulations of data are required. However, the user is given the option, at the end, to perform any desired additional manipulations of data.
- The MSRCR algorithm is able to ensure that details are not lost when illumination conditions are not optimal (i.e., in shadowed or brightly illuminated zones of an image, as shown in the figure). The algorithm also en-

forensic imaging, and editing of motion pictures.

This work was done by Glenn A. Woodell and Daniel J. Jobson of Langley Research Center and Zia-ur Rahman of TruView Imaging Co. For further information, please contact Mr. Zia-ur Rahman, telephone (757) 766-5850 or send e-mail to zrahman@truview.com. For information on Photoflair product see [www.truview.com](http://www.truview.com), for information on NASA technology see [www.dragon.larc.nasa.gov/retinex](http://www.dragon.larc.nasa.gov/retinex).

In accordance with Public Law 96-517, the contractor has elected to retain title to this invention. Inquiries concerning rights for its commercial use should be addressed to

TruView Imaging Co.  
10 Basil Sawyer Drive  
Hampton, VA 23666-1393

Refer to LAR-15514, volume and number of this NASA Tech Briefs issue, and the page number.



### **Analysis of Designs of Space Laboratories**

A report presents a review of the development of laboratories in outer space, starting from the pioneering Skylab and Salyut stations of the United States and the former Soviet Union and progressing through current and anticipated future developments. The report includes textual discussions of space-station designs, illustrated with drawings, photographs, and tables. The approach taken in the review was not to provide a comprehensive catalog of each space laboratory and every design topic that applies to it, but, rather, to illustrate architectural precedents by providing examples that illustrate major design problems and principles to be applied in solving them. Hence, the report deemphasizes information from the most recent space-station literature and concentrates on information from original design reports that show how designs originated and evolved. The most important contribution of the review was the development of a methodology, called “units of analysis,” for identifying and analyzing design issues from the perspectives of four broad domains: laboratory science, crew, modes of operations, and the system as a whole.

*This work was done by Marc M. Cohen of Ames Research Center. Further information is contained in a TSP (see page 1). ARC-14965*

### **Shields for Enhanced Protection Against High-Speed Debris**

A report describes improvements over the conventional Whipple shield (two thin, spaced aluminum walls) for protecting spacecraft against high-speed impacts of orbiting debris. The debris in question arises mainly from breakup of older spacecraft. The improved shields include exterior “bumper” layers composed of hybrid fabrics woven from combinations of ceramic fibers and high-density metallic wires or, alternatively, completely metallic outer layers composed of high-strength steel or copper wires. These

shields are designed to be light in weight, yet capable of protecting against orbital debris with mass densities up to about 9 g/cm<sup>3</sup>, without generating damaging secondary debris particles. As yet another design option, improved shields can include sparsely distributed wires made of shape memory metals that can be thermally activated from compact storage containers to form shields of predetermined shape upon arrival in orbit. The improved shields could also be used to augment shields installed previously.

*This work was done by Eric L. Christiansen and Justin H. Kerr of Johnson Space Center. Further information is contained in a TSP (see page 1).*

*This invention is owned by NASA, and a patent application has been filed. Inquiries concerning nonexclusive or exclusive license for its commercial development should be addressed to the Patent Counsel, Johnson Space Center; (281) 483-0837. Refer to MSC-22330.*

### **Study of Dislocation-Ordered In<sub>x</sub>Ga<sub>1-x</sub>As/GaAs Quantum Dots**

A report describes an experimental study of dislocation-induced spatial ordering of quantum dots (QDs) comprising nanometer-sized In<sub>x</sub>Ga<sub>1-x</sub>As islands surrounded by GaAs. Metastable heteroepitaxial structures were grown by molecular-beam epitaxy of In<sub>x</sub>Ga<sub>1-x</sub>As onto n<sup>+</sup>GaAs and semi-insulating GaAs substrates. Then the structures were relaxed during a post-growth annealing/self-organizing process leading to the formation of surface undulations that acted as preferential sites for the nucleation of QDs. Structural effects of annealing times and temperatures on the strain-relaxed In<sub>x</sub>Ga<sub>1-x</sub>As/GaAs and the subsequent spatial ordering of the QDs were analyzed by atomic-force microscopy and transmission electron microscopy. Continuous-wave spectral and time-resolved photoluminescence (PL) measurements were performed to study the effects, upon optical properties, of increased QD positional ordering, increased QD uniformity, and proximity of QDs to arrays of dislocations. PL spectral peaks of ordered QD structures formed on strain-relaxed In<sub>x</sub>Ga<sub>1-x</sub>As/GaAs layers were

found to be narrower than those of structures not so formed and ordered. Rise and decay times of time-resolved PL were found to be lower at lower temperatures — apparently as a consequence of decreased carrier-transport times within the barriers surrounding the QDs.

*This work was done by Rosa Leon of Caltech for NASA's Jet Propulsion Laboratory. Further information is contained in a TSP (see page 1). NPO-30691*

### **Tilt-Sensitivity Analysis for Space Telescopes**

A report discusses a computational-simulation study of phase-front propagation in the Laser Interferometer Space Antenna (LISA), in which space telescopes would transmit and receive metrological laser beams along 5-Gm interferometer arms. The main objective of the study was to determine the sensitivity of the average phase of a beam with respect to fluctuations in pointing of the beam. The simulations account for the effects of obscurations by a secondary mirror and its supporting struts in a telescope, and for the effects of optical imperfections (especially tilt) of a telescope. A significant innovation introduced in this study is a methodology, applicable to space telescopes in general, for predicting the effects of optical imperfections. This methodology involves a Monte Carlo simulation in which one generates many random wavefront distortions and studies their effects through computational simulations of propagation. Then one performs a statistical analysis of the results of the simulations and computes the functional relations among such important design parameters as the sizes of distortions and the mean value and the variance of the loss of performance. These functional relations provide information regarding position and orientation tolerances relevant to design and operation.

*This work was done by Miltiadis Papalexandris of Caltech and Eugene Waluschka of Goddard Space Flight Center for NASA's Jet Propulsion Laboratory. Further information is contained in a TSP (see page 1). NPO-30709*





